SOCIAL AND ETHICAL ISSUES IN COMPUTING.

See SOCIAL AND ETHICAL ASPECTS OF INFORMATION TECHNOLOGY.

SOFT MAGNETIC MATERIALS

Soft magnetic materials (SMMs) are alloys used as efficient flux multipliers. They are basic components in a wide class of electric and electronic devices, including motors, generators, transformers, and a host of apparatus, ranging from household appliances to highly sophisticated scientific equipment. The present market for SMMs is globally estimated at around 8 million tons, for a value close to US$10 billion. SMMs were the first magnetic materials to be actively investigated, developed, and applied at the beginning of the electrotechnical era. At the end of the 19th century, the abundance of iron and the industrial steel practice of the time could combine to produce the large amount of low-priced low carbon steel laminations required to satisfy the rapidly expanding demand for generation, transportation, and use of the electric energy. The first breakthrough in the history of SMMs occurred at the turn of the century, when Hadfield, Barrett, and Brown proved that the addition of around 2% in weight of silicon definitely improved the magnetic properties of low-carbon steels, leading, in particular, to strongly reduced energy losses (1). In spite of their high costs, the Fe–Si laminations found their way into applications, especially as transformer cores. The rewards in terms of energy savings were high: It was estimated that in the first 17 years of its use, Fe–Si saved more than US$300 million for the American electrical industry. Our present knowledge of ferromagnetism permits us to assess in retrospect the progress achieved by the trial-and-error method in

the SMM properties during the first decades of the century. Several breakthrough discoveries were made as a result of empirical approaches and investigations, in advance of any reasonable theoretical framework. This is the case with the extrasoft Fe–Ni alloys, originating from the studies of G. W. Elmen in the years 1915 to 1920 (2), and the grain-oriented Fe–Si laminations that N. P. Goss developed in the early 1930s, without recognizing the extraordinary nature of the crystallographic texture he could produce by his process (3). The development of ferrites, magnetically soft Fe-based oxides stemming from the ancient magnetite compound Fe_3O_4, was accomplished in the 1940s, mainly by Snoek (4), following attempts dating back to the first decade of the century. The landscape of SMMs was eventually enriched by truly new materials in the 1970s, with the discovery and the industrial production of amorphous alloys.

The magnetic properties involved in any kind of application are embodied by the hysteresis loop. Materials are classified according to a number of hysteresis loop parameters, by which the material quality can be assessed. The main parameters of interest, shown in Fig. 1, are the coercive field H_c, the remanent induction B_r, the peak permeability $\mu = B_p/H_p$, and the loop area $W_h = \oint H \cdot dB$. W_h represents the energy dissipated per unit volume upon a complete magnetization cycle. All of these parameters depend in a complex way on the composition and the structural features of the material. The composition determines the values of the intrinsic magnetic parameters, like the saturation magnetization, the magnetic anisotropy constants, and the magnetostriction constants, which, in turn, affect the magnetization process in a way related to the specific structural properties of the material–that is, crystallographic texture, grain size, impurities, and lattice
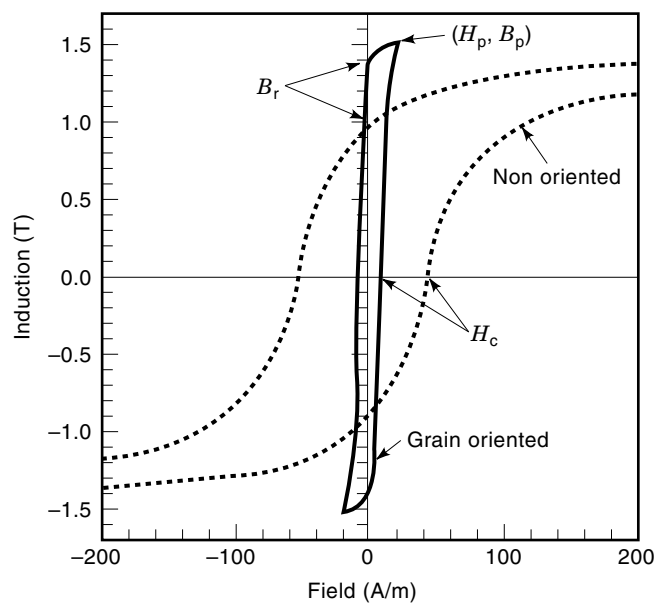
defects. By their very definition, SMMs should magnetize as easily as possible. In practice, we classify as soft those materials having coercivities lower than 10^2 A/m, which implies typical values of the relative permeability ($\mu_r = \mu/\mu_0$, where $\mu = B_p/H_p$ and μ_0 is the permeability of the vacuum) in the range of 10^3 and higher. Extrasoft magnets have been obtained, where H_c and μ_r can reach values as extreme as a few 10^{-1} A/m and some 10^6 A/m, respectively. It should be stressed, however, that materials of potential interest to applications are evaluated against a number of additional properties, like thermal and structural stability, stress sensitivity of the magnetic parameters, mechanical properties and machinability, and heat conductivity. The final acceptance of a material as relevant or promising for certain applications results from a broad-range cost–benefit evaluation of all these properties.

The key feature of SMMs, as of any other magnetic material, is that they are subdivided into magnetic domains. Each domain is a region in which the magnetization is uniform and points along a direction that changes from domain to domain. The overall magnetization of a macroscopic piece of SMM is the result of an average over many domains, and as such its value is mainly dictated by the relative volume and orientation of the domains present in the material. The orientation of the magnetization inside a given domain is usually limited to a small number of privileged directions, resulting from the presence of some form of anisotropy. The strength and the symmetry of anisotropy effects play a leading role in determining the magnetic properties. The strength is usually summarized by a suitable anisotropy constant, K, which has the dimensions of an energy density (J/m^3). The symmetry can be uniaxial, cubic, or more complex, depending on the material. The magnetization process of an SMM typically occurs by means of two microscopic mechanisms: motion of the interface layers separating neighboring domains, known as domain walls (DWs), and uniform rotation of the magnetization inside each domain. Coercivity and hysteresis are determined by the frictional forces that the DWs, acted on by the applied field, have to overcome during their motion. Such forces basically originate from the defective structure of the material and balance the pressure exerted on the walls by the applied field. The coercive field measures the typical field strength at which DWs are unpinned from defects and a substantial part of the magnetization in the material is reversed. Energy is lost in this process, and magnetic hysteresis is accordingly observed. The theoretical assessment of magnetic coercivity is chiefly due to Néel (5), who quantitatively accounted for the role of structural defects and random internal stresses in hindering the motion of the DWs. The hindering effect is controlled by the value of the anisotropy constant, which means that, in general, coercivity tends to increase with the strength of anisotropy effects. However, for a given anisotropy, coercivity still exhibits a substantial dependence on the microstructure, which can even change the magnetic behavior of a given material from soft to hard.

In polycrystalline SMMs, like low-carbon steels and silicon steels, the condition for having a low coercive field is that they should be as free as possible of precipitates, voids, and lattice defects, and at the same time they should have a low density of grain boundaries and a favorable distribution of grain orientations. This last requirement follows from the existence of a specific form of anisotropy known as magnetocrystalline anisotropy, which makes particular directions of the crystal

Figure 1. Quasi-static magnetic hysteresis loops measured at 1.5 T peak induction in typical grain-oriented (GO) and nonoriented (NO) Fe–(3 wt%)Si laminations. H_c and B_r denote the coercive field and the remanent induction, respectively. The softer GO alloys are characterized by a sharply defined (110)[001] crystallographic texture. The area of the loop, which represents the specific energy loss per cycle (J/m^3) roughly scales with the value of the coercive field.

lattice energetically favorable for the magnetization (easy axes). In iron the edges of the lattice cubic cell (⟨100⟩ axes) are easy axes, and the associated anisotropy constant is $K = 4.9 \times 10^4$ J/m³. The coercivity tends to be lower when all grains have one of their easy axes close to the applied field direction. This is the condition realized in grain-oriented silicon steels. Conversely, Fe and low-carbon steels give a good illustration of the role of microstructural defects. Very low coercive fields, down to few amperes per meter, can be obtained in well-annealed, high-purity Fe. On the contrary, in carbon steels with C concentration around 1 wt%, a defective structure of cementite (Fe_3C) and graphite precipitates or martensitic domains can be induced by specific thermal treatments, which strongly hinders the DW motion and leads to H_c values typical of hard magnets, in the range of several 10^4 A/m. Fe–Ni alloys with composition around $Fe_{25}Ni_{75}$, amorphous alloys, and nanocrystalline alloys are SMMs where very low values of the coercive field are obtained because the anisotropy is orders of magnitude lower than in Fe. In Ni–Fe alloys, one can exploit the transition from positive (high Fe concentration) to negative (high Ni concentration) values of the anisotropy constant to adjust the composition in a way to achieve vanishing anisotropy. In amorphous and nanocrystalline materials, the same effect follows from the fact that these materials are aggregates of elementary structural units, whose size ranges from few atomic spacings to few tens of nanometer. The characteristic length controlling magnetic effects, represented by the DW thickness, is much larger than the size of these structural units, so that the effective magnetocrystalline anisotropy sensed by the DWs in their motion is the result of an average over many structural units oriented at random. The overall effect practically balances out to zero, and no large-scale preferential directions exist for the magnetization (6). Even when the magnetocrystalline anisotropy is averaged out to zero, a substantial anisotropy can still be produced in magnetostrictive alloys by the magnetoelastic coupling between stress and magnetization. In particular, the uniaxial anisotropy induced by a tensile/compressive stress of intensity σ turns out to have a strength $K = \frac{3}{2}\lambda_s\sigma$, where the constant λ_s, the so-called saturation magnetostriction, is a measure of the strength of the coupling between stress and magnetization. A low magnetostriction is thus required to minimize the stress anisotropies. A material lacking large-scale anisotropy, besides being expectedly very soft, is very versatile, because its properties can be adjusted to specific needs by means of induced anisotropies. A classical case is represented by the Fe–Ni alloys annealed and cooled under a large external field, where magnetic anisotropies of the order of some 10^2 J/m³ can be induced along the applied field direction. The underlying physical process is the so-called directional order, where Fe–Fe and Ni–Ni atomic pairs rearrange in such a way that after the annealing they are preferentially found parallel to the direction of the magnetization, with the alloy nonetheless maintaining the character of random solution. Induced anisotropies can be obtained also in amorphous and nanocrystalline alloys, by thermomagnetic treatments that favor structural rearrangements in the materials. An example of the evolution with field annealing of the hysteresis loop of an amorphous alloy is shown in Fig. 2. As previously mentioned, polycrystalline materials are characterized by a distribution of easy axes, which, according to the specific domain structure of the sample, creates
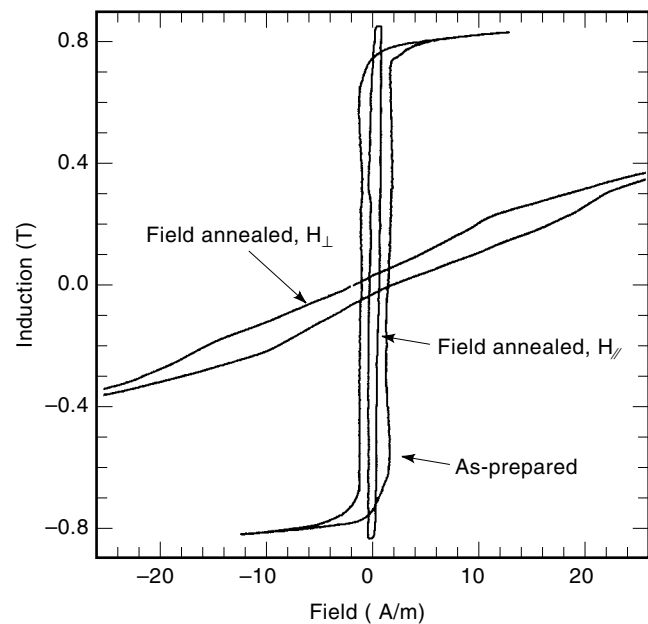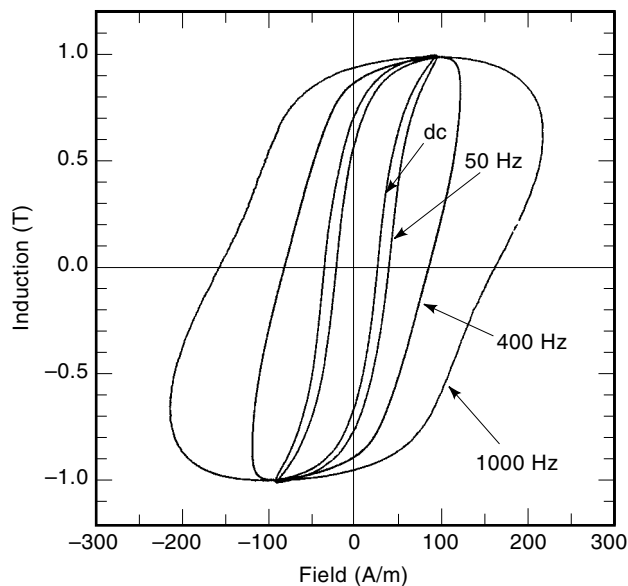

Figure 2. Quasi-static magnetic hysteresis loop in $Co_{71}Fe_4B_{15}Si_{10}$ amorphous ribbons: as-prepared by rapid solidification; after annealing (1000 s at 300°C) under longitudinal saturating field $H_\parallel$; after annealing (3000 s at 220°C) under transverse field $H_\perp$. The field annealing treatments induce a uniaxial anisotropy with easy axis directed along the field direction.
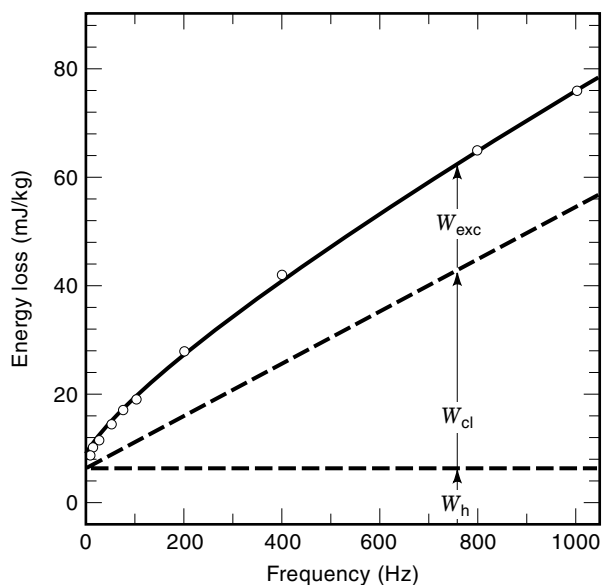
a corresponding dispersion of the magnetization directions. Thus, an applied field not only provides a pressure on the DWs, but it exerts a torque on the magnetic moments within the domains, which is balanced by an opposing torque provided by the anisotropy. The field required to overcome the anisotropy torque is of the order of $2K/I_s$, where I_s the saturation magnetization. In Fe and Fe-based alloys this field is in the range of some 10^4 A/m. Consequently, the rotation of the magnetization starts to contribute to the magnetization reversal of SMMs when most of the DW displacements have already taken place, eventually bringing the material to the saturated state. In the low and extra-low anisotropy materials, like the Fe–Ni and the amorphous alloys, DW motion and magnetization rotation processes overlap somewhat, as a consequence of the comparable values attained by the ratio $2K/I_s$ and the coercive field H_c. A case in point is provided by the sheared hysteresis loop exhibited by the transversally field annealed amorphous alloy shown in Fig. 2. In this case, magnetization rotations predominantly contribute to the whole magnetization reversal, resulting into a roughly linear B–H curve.

SMMs are mostly used in alternating current apparatus, from 50 Hz to the megahertz region. Eddy currents generated by the magnetic flux variations are responsible for two main phenomena: shielding of the interior of the magnetic core from the applied field and loss of energy by the Joule effect. Since the end of the last century, laminated magnetic steel cores have been adopted in electric machines in order to restrain both effects, which remain, however, difficult to assess in a quantitative way, due to the intrinsic nonlinear behavior of ferromagnets. Early quantitative analyses of this problem were carried out under the drastically simplified assumption

that the material could be assimilated to a homogeneous medium with no hysteresis. It was with the fundamental studies of DW dynamics in Fe–Si single crystals carried out by H. J. Williams, W. Shockley, and C. Kittel in 1950 (7) that substantial progress in understanding and predicting energy losses could be achieved. The general phenomenology of losses is summarized in Fig. 3, showing the evolution versus the magnetizing frequency f of the shape and the area of the hysteresis loop of a typical Fe–Si lamination. This figure puts in evidence that (a) the energy loss W tends to a limiting value W_h when $f \rightarrow 0$, (b) W exhibits a nonlinear increase with f, (c) the dynamic loss contribution which adds to W_h at the frequency f is always larger than the value predicted by the solution of Maxwell's equations for a homogeneous medium (classical approach). Of fundamental importance for the study of loss phenomena is the concept of loss separation: The energy loss per cycle at a given frequency is assumed to be the sum of three different contributions, according to the equation

$$W = W_h + W_{cl} + W_{exc} \tag{1}$$

where W_h is the hysteresis loss, which is frequency-independent by definition, W_{cl} is the classical loss, calculated from Maxwell's equations, and W_{exc} is the so-called excess loss. The three loss components are related to different physical mechanisms acting in the material. The classical loss W_{cl} is a sort of background contribution, always present and independent of any structural feature. One finds from Maxwell's equations that the specific loss per cycle, expressed in joules per cubic meter, is given by

$$W_{cl} = \frac{\pi^2}{6} \cdot \sigma B_p^2 d^2 f \tag{2}$$

in a lamination of thickness d and conductivity σ, magnetized under sinusoidal induction of peak value B_p, under the assumption of complete flux penetration in the lamination cross section. The behavior predicted by Eq. (2) in the previous Fe–Si lamination is shown in Fig. 3. The other terms, W_h and W_{exc}, that are added to W_{cl} derive from the existence of magnetic domains and from the inherently discrete nature of the magnetization process. Flux reversal is concentrated at moving DWs; and even under quasi-static excitation, eddy currents arise, because the DW displacements, hindered by the material imperfections, occur in quite a discontinuous fashion (Barkhausen effect). Very intense and short-lived ($\sim 10^{-9}$ s) current pulses are generated, closely localized around the jumping wall segments, which are the eventual source of W_h. The theory shows that the energy dissipated in the material by this mechanism is, as the coercivity should be, a volume effect, independent of the conductivity and the geometry of the material. The excess loss W_{exc} is instead the consequence of the large-scale motion of DWs. Theoretical considerations show that in most SMMs and in particular in silicon steels, the following expression holds to a good approximation:

$$W_{exc} = k_{exc} \cdot \sqrt{\sigma f} \cdot B_p^{3/2} \tag{3}$$

where k_{exc} is a parameter taking into account the actual domain pattern present in the lamination and its relationship with the material microstructure (8). k_{exc} is a measure of the inhomogeneity of the magnetization process and becomes vanishingly small in the limiting ideal case of magnetically uniform material. Consequently, in order to minimize the energy losses in soft magnetic laminations, we not only need to reduce thickness and conductivity, as suggested by Eq. (2), but we also have to control microstructural features, like, for instance, grain size and crystallographic texture, which act on the static coercivity as well as on the DW dynamics. This

(a)

(b)

Figure 3. Hysteresis loop shape (a) and specific loss per cycle (mJ/kg) (b) versus magnetizing frequency in nonoriented (NO) Fe–(3 wt%)Si laminations, 0.35 mm thick. Measurements were performed at a fixed peak induction of 1 T under controlled sinusoidal induction waveform. The loss per cycle is proportional to the area of the hysteresis loop. Loss separation is illustrated in (b), where the three components W_h (hysteresis), W_{cl} (classical), and W_{exc} (excess) are singled out.
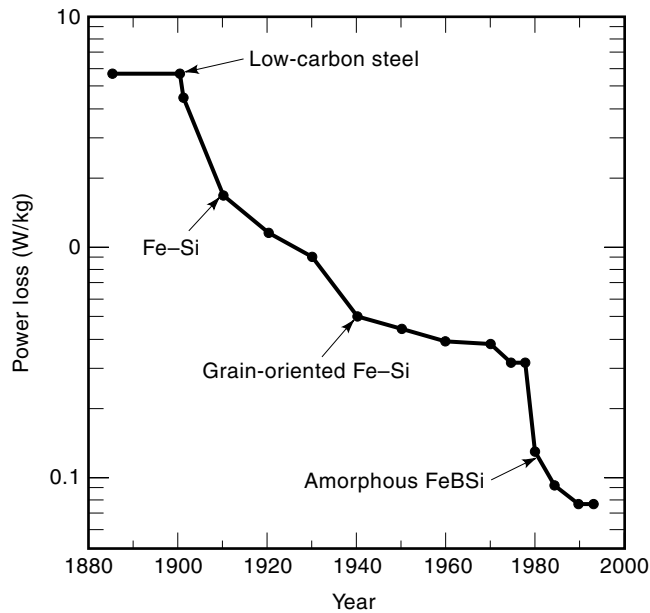
Figure 4. Progress along a century of the record loss figures of laminations for transformer cores. $B_p = 1$ T; $f = 50$ Hz.

data. Published standards are periodically revised, as required by the advances in materials, applications, and measuring techniques. The whole subject of specifications and measurements in magnetic alloys and steels is covered by the IEC Standard Series 404.

IRON, LOW-CARBON STEELS, AND SILICON STEELS

Iron is referred to as "high-purity" when the total concentration of impurities (typically C, N, O, Mn, P, S, Si, Al) does not exceed some hundred parts in 10^{-6} (ppm). It is otherwise referred to as "low-carbon steel" or "non-alloyed" steel. When soluble elements like Si and Al are deliberately introduced, typically in the range of a few percent, we shall more aptly speak of "silicon steels." The chief benefit obtained by the addition of Si in Fe is represented by the notable increase of the electrical resistivity, of the order of 5×10^{-8} $\Omega \cdot$m per soluted atomic percent, and the ensuing reduction of the eddy current losses [Eqs. (2) and (3)]. This was already recognized by early users of Fe–Si laminations at the start of the century, although the poor control of the C content could somewhat mask the prospective performances of this product with respect to the mild steels in use at that time. There are further properties that take advantage of Si alloying, like the decrease of the magnetocrystalline anisotropy constant K, which is reflected in a lower coercivity, and the increase of the yield strength, which favors material handling and machining. In addition, inspection of the Fe–Si phase diagram shows that above about 2 wt% Si the $\alpha \rightarrow \gamma$ transition [from body-centered cubic (bcc) to face-centered cubic (fcc) structure] no longer takes place and complete freedom in thermal treatments exists in this respect. The chief factors against substantial addition of Si are the reduction of the saturation magnetization and the fact that there is no practical way of achieving laminations with more than about 4 wt% Si by conventional rolling processes. The heterogeneous formation of FeSi and Fe_3Si ordered phases leads in fact to severe material embrittlement. The behavior of resistivity, anisotropy constant, saturation magnetization, and yield stress versus Si concentration is shown in Fig. 5.

Iron and Low-Carbon Steels

Very pure iron is of basic physical interest, but it is seldom used in applications. It exhibits, besides high costs, relatively

is the chief objective of the metallurgical processes that have been developed in the last decades, and that have produced steady improvements in the properties of materials and a remarkable array of applicative options. A hint to the progress achieved through a century is provided in Fig. 4, which shows the decrease over time of the record loss figure, measured at power frequency, in soft magnetic laminations for transformer cores.

A list of representative SMMs is given in Table 1. The specifications for SMMs and the measurement of their direct-current (dc) and alternating-current (ac) magnetic properties are provided in standards issued by national (e.g., ASTM, DIN, JIS) and international (e.g., IEC) bodies. The codification imposed by these standards, guiding through the various stages of materials production, characterization, and application, is indispensable to producers and users. They impose, for instance, tight procedures for magnetic measurements, in order to guarantee reproducibility and traceability of the

Table 1. Representative Soft Magnetic Materials and Typical Values of Some Basic Magnetic Parameters

Soft Magnetic Material	Composition	μ_{max}	H_c (A/m)	I_s (T)
Fe	Fe100	$3–50 \times 10^3$	1–100	2.16
NO Fe–Si	Fe(>96)–Si(<4)	$3–15 \times 10^3$	30–80	1.98–2.12
GO Fe–Si	Fe97–Si3	$20–80 \times 10^3$	4–15	2.03
Sintered powders	Fe99.5–P0.5	$0.2–2 \times 10^3$	100–500	1.65–1.95
Permalloy	Fe16–Ni79–Mo5	5×10^5	0.4	0.80
Permendur	Fe49–Co49–V2	2×10^3	100	2.4
Ferrites	$(Mn,Zn)O \cdot Fe_2O_3$	3×10^3	20–80	0.2–0.5
Sendust	Fe85–Si9.5–Al5.5	50×10^3	5	1.70
Amorphous (Fe-based)	$Fe_{78}B_{13}Si_9$	10^5	2	1.56
Amorphous (Co-based)	$Co_{71}Fe_4B_{15}Si_{10}$	5×10^5	0.5	0.86
Nanocrystalline	$Fe_{73.5}Cu_1Nb_3Si_{13.5}B_9$	10^5	1	1.24

$\mu_{max} \equiv$ maximum dc relative permeability; $H_c \equiv$ coercive field; $I_s \equiv$ saturation magnetization at room temperature. The composition is given in wt%, but for the amorphous and nanocrystalline alloys, where it is expressed in at%.
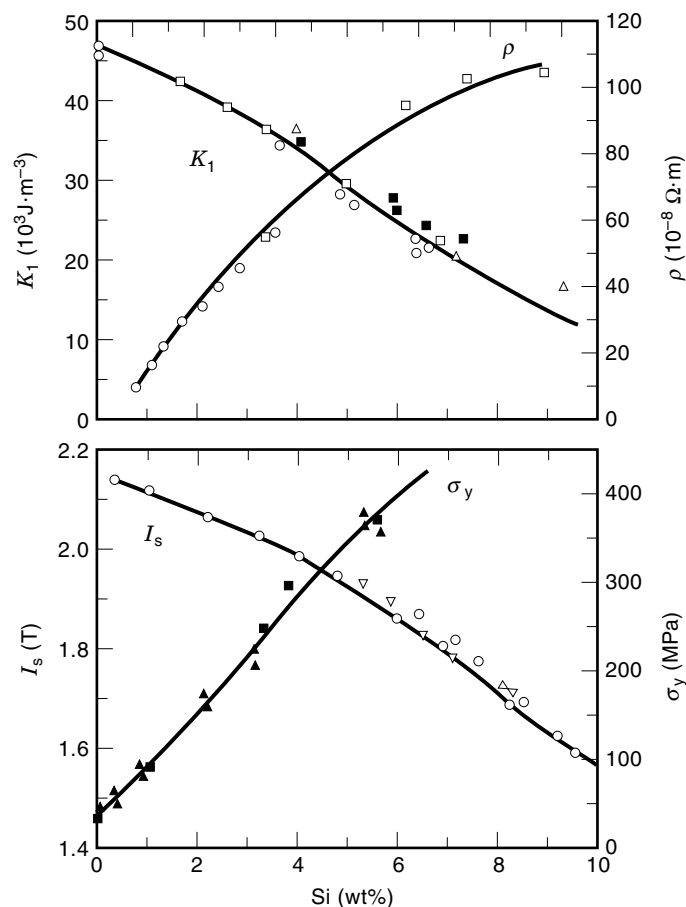
Figure 5. Dependence of magnetocrystalline anisotropy constant K_1, electrical resistivity ρ, saturation magnetization I_s, and yield stress σ_y versus Si concentration in Fe–Si alloys.

To obtain high-purity iron, it is practical to refine conventionally pure iron (e.g., ARMCO type) after decarburization and purification in the molten state. Refining methods include prolonged annealing (24 h to 48 h) at 1480°C in pure H_2 atmosphere (Cioffi process), zone melting, and levitation melting. By these methods, some 20 ppm to 30 ppm maximum total impurity content can be ultimately reached, with C and N less than 10 ppm (see Table 2). Record permeabilities $\mu_r \sim 10^6$ and coercivities $H_c \sim 2$ A/m have been obtained by this method. The total carbon content in low-carbon steels is generally limited to about 0.1 wt% to 0.005 wt%, with a comparable content of other impurities (Table 2). Low-carbon steels for magnetic applications are generally produced in sheet geometry, through a sequence of hot and cold rolling passes. In the case of low-cost materials, heat and mechanical treatments are limited to those necessary to reach the final sheet thickness, which may range from 0.50 mm to 0.85 mm. Better magnetic performance can be achieved by decarburization, a final process where the carbon concentration can be typically reduced to less than 50 ppm by annealing in wet hydrogen atmosphere at temperatures around 800°C. The main detrimental effect of C is magnetic aging—that is, the increase of coercivity over time consequent to the formation of cementite precipitates, which give rise to substantial domain wall pinning. Aging may represent a real threat in actual magnetic cores, where operating temperatures of 50° to 100°C are common. Figure 6 shows that in low-carbon steels with C concentrations as low as 45 ppm a potential for aging still exists (9). Nitrogen can equally induce aging, but it can be partly stabilized by the formation of AlN precipitates. These, however, may adversely affect the grain texture during recrystallization annealing, by favoring the growth of unfavorable {111} planes. Such an effect can be largely avoided by controlled addition of either B ($\sim$30 ppm) or Zr (0.07 wt%) (10). Reduction of the C, N, and S concentrations in the range of 20 ppm to 30 ppm can alternatively be obtained, in high-quality steels, by vacuum degassing of the melt. This makes unnecessary the final decarburization anneal, with beneficial effects on the production costs. The $\alpha \rightarrow \gamma$ transition takes place in pure Fe at 910°C, and the final thermal treatments are thus preferably made at lower temperatures, which may limit the range of attainable grain sizes and crystallographic textures. Low-carbon steels are generally delivered as semiprocessed products. Starting from the hot rolling stage, the laminations are subjected in sequence to pickling, cold rolling to final thickness, intermediate annealing for recrystallization. This is followed by temper rolling, a 3% to 5% cold reduction, which imparts the mechanical hardness required for subsequent punching by the user. The punched laminations are then subjected to decarburization and grain growth annealing, eventually followed by controlled surface oxidation

inferior mechanical properties, which make it unsuitable for precise lamination cutting and punching. Low-carbon steels, with typical C content below 0.1 wt%, find large-scale applications as low-grade, low-cost magnetic cores in direct current (dc) and alternating current (ac) devices. Together with the silicon steels, they cover at present nearly 80% of the world tonnage of soft magnetic materials. Growing concern for environmental issues and rising energy costs have stimulated the development of improved low-carbon steels, which can be used in the design of more efficient electric machines. Materials of higher magnetic grade can be obtained by raising to some extent the Si content (up to about 1 wt%), by lowering the total content of impurities such as sulfides, nitrides, and carbides, by increasing the grain size, and by controlling the crystallographic texture.

Table 2. Typical Impurities and Their Concentrations (wt ppm) in Several Grades of Iron and in Low-Carbon Steel

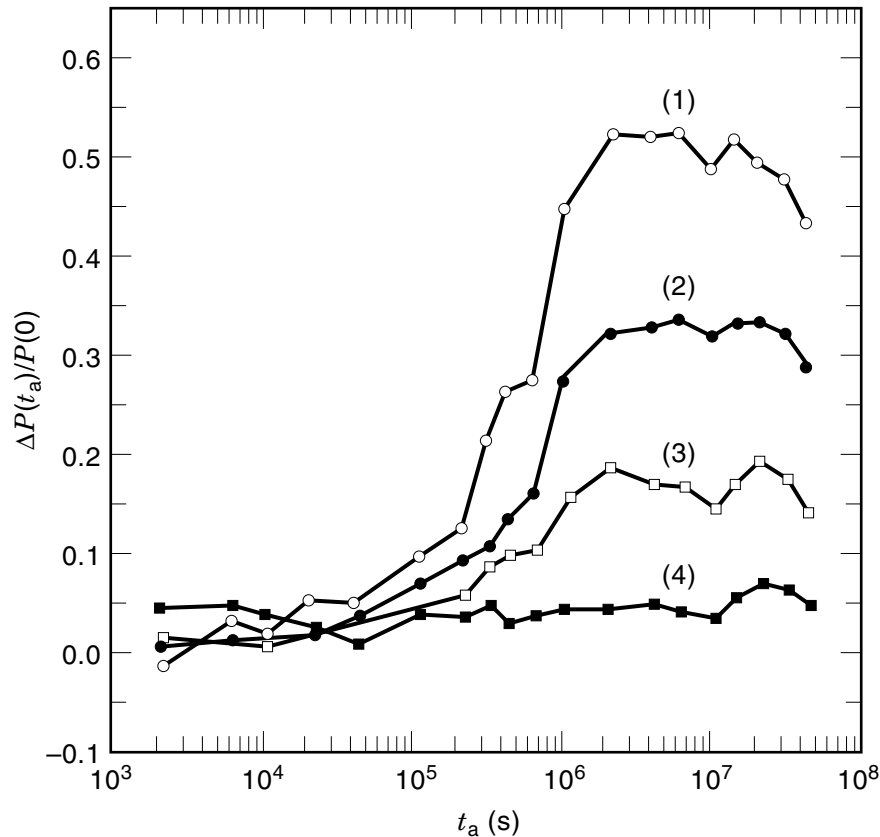| Iron Type	C	N	O	Mn	P	S	Si	Cu	Ni
ARMCO	150	20	150	280	50	250	30	150	
Electrolytic	40	100	100	15	20	30	30	40	10
H_2-treated	50	10	30	280	40	<30			
Zone-refined	7	<10	2	0.5	<0.1	0.2		1.5	0.50
Low-carbon steel	50–1000	30–200	20–100	5×10^3	200–1000	50–300	10^3–10^4	100	

Figure 6. Relative increase $\Delta P(t_a)/P(0)$ of the power loss at 50 Hz and 1.5 T in a low-carbon steel lamination (Si 0.3 wt%), after aging at 150°C for the time t_a. Curves (1) to (4) refer to the following C concentrations (wt ppm): 156, 57, 45, 21. (Data taken from Ref. 9.)

("bluing"), to ensure acceptable interlaminar insulation in the core. One notable consequence of temper rolling is a somewhat exaggerated grain growth upon final annealing, which overcomes to some extent the limitations imposed on the upper treatment temperatures by the $\alpha \rightarrow \gamma$ transition. Low-carbon steel performance is best described in terms of ac magnetic properties at 50 Hz or 60 Hz. In the absence of purification treatments and significant Si content, ac losses at 60 Hz and 1.5 T can reach some 15 W/kg in 0.65-mm-thick laminations, with relative permeability μ_r = 500 to 1000. The addition of ~1 wt% Si, together with better composition control, may contribute to lowering the power loss to less than 8 W/kg, with $\mu_r \sim 2000$ (see Fig. 7) (11). However, the introduction of Si decreases the saturation magnetization, which may be somewhat detrimental to permeability. Therefore, it is preferable, whenever possible, to improve loss performance by the use of clean materials. In particular, with the development of clean ultra-low-carbon steels, which do not need the decarburizing treatment, it has become possible to develop coated semiprocessed materials, which combine improved loss and permeability behavior ($P \sim 4$ W/kg and $\mu_r \sim 3000$ at 1.5 T and 50 Hz in 0.50 mm thick laminations) with excellent punching performance.

Pure Fe and nonalloyed steels find applications as cores of dc electromagnets, where one exploits their high saturation magnetization in producing strong fields. Typical ac applications are relays, lamp ballasts, fractional power motors, and small transformers, where performance is needed at low price. It is known that in small motors (power less than 1 kW to 2 kW), where the limited size imposes high induction values in the stator teeth, copper losses tend to predominate over
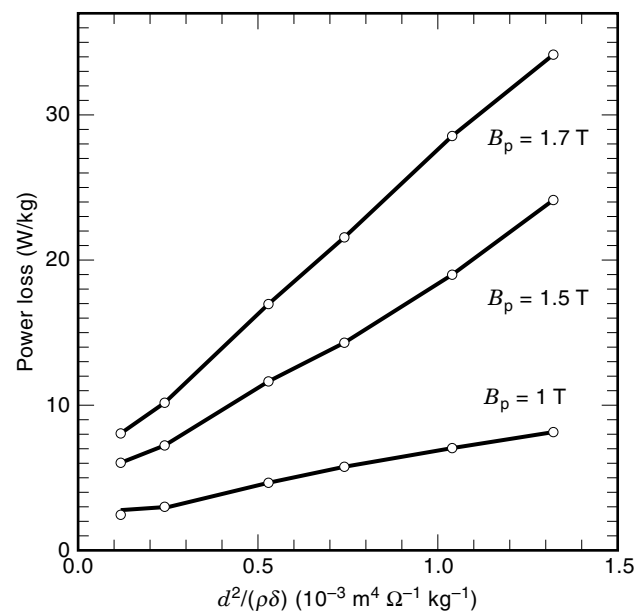

Figure 7. Specific power loss in low-carbon steel laminations as a function of the quantity $d^2/\rho\delta$, where d, ρ, and δ represent the lamination thickness, resistivity, and density, respectively. Measurements refer to a magnetizing frequency of 60 Hz and to three different peak inductions. The reported data are representative of the behavior observed in different samples, having the following ranges of solute concentrations (wt%): Mn 0.34–0.99, P 0.002–0.22, Si 0.02–0.54, Al 0.003–0.53, S < 0.004, O < 0.05. (Data taken from Ref. 11.)

iron losses. The solution offered by nonalloyed steels, with their high values of permeability at high inductions and affordable price, represents a good compromise between the requirements of costs and machine efficiency. Optimal product performance is eventually obtained through proper design considerations. For applications in the kilohertz range soft iron powder cores are often used. They are obtained starting from iron particles of 50 μm to 100 μm size, prepared by milling or electrolytic deposition and insulated by surface treatment. The particles are compressed as cores of the desired shape, which are heat-treated and coated by protective painting. Being finely subdivided and, consequently, characterized by a distributed air gap, the iron powder cores exhibit a sheared hysteresis loop and relatively low values of permeability ($\mu_r \sim 100$). The lack of any large-scale electrical conductivity gives largely reduced dynamic losses with respect to the bulk samples, and a frequency independent permeability is consequently obtained up to 50 kHz to 100 kHz. Applications for iron powder cores include loading coils, pulse transformers, inductors in switching mode power supplies, and small high-speed motors.

Nonoriented Silicon Steels

Nonoriented (NO) Fe–Si alloys are SMMs with an approximately isotropic grain texture. They cover the medium and high quality range of SMMs for applications in electrical rotating machines, where good isotropic magnetic properties are required. They come in a variety of grades, the higher ones being associated with higher Si content. The Si concentration can vary between 1 wt% and 3.7 wt% and some percentage of Al (0.2 wt% to 0.8 wt%) and Mn (0.1 wt% to 0.3 wt%) is usually added, by which the alloy resistivity is further increased without impairing the mechanical properties. The lower-grade NO laminations (up to ~2 wt% Si) are produced in the semiprocessed state and follow the same thermomechanical history of low-carbon steels, with final thickness ranging between 0.65 mm and 0.50 mm. The higher grades are instead fully processed materials. They are obtained according to the following procedure. The hot-rolled sheets (thickness 2.3 mm to 1.8 mm) are cold-rolled to intermediate gauge, annealed at 750° to 900°C, reduced to the final gauge of 0.65 mm to 0.35 mm, and subjected to a recrystallization and decarburization anneal at 830° to 900°C and to a final grain-growth anneal at 850° to 1100°C. A single-stage cold reduction is a basic variant of this process. A phosphate-based or chromate-based coating is then applied, which not only provides the necessary interlaminar insulation, but also ensures good lamination punchability. Contrary to the case of semifinished products, no stress relief treatment is applied in general after sheet punching. By acting on the composition and the preparation methods, with the help of improved understanding of the role of the structural parameters on the loss and permeability behavior, a wide range of NO steels with variable quality has been made available to the users. The top commercial grades have around 4 wt% (Si + Al) concentration and, with a gauge of 0.35 mm to 0.50 mm, they exhibit a loss figure $W_{15/50}$ of 2.10 W/kg to 2.30 W/kg at 1.5 T and 50 Hz, and an induction $B_{25} = 1.55$ T at 2500 A/m. Nonoriented Fe–Si alloys are preferentially employed in medium- and high-power rotating machines, whereas, as previously stressed, low-carbon steel laminations are preferred in small apparatus. The highest

efficiency ($>95\%$) is sought in large machines, not only to save energy, but also to avoid overheating and shortened machine life span. The development of improved alloys is related to the control of a number of structural parameters, namely impurities, grain size, crystallographic texture, surface state, and residual and applied stresses. Several tens of parts per million concentrations of impurities like C, N, S, and O tend to increase coercivity and losses (see Figs. 6 and 8). They can do this directly, by forming precipitates that act as pinning centers for the domain walls, and indirectly, by adversely affecting grain growth and texture. The role of grain size is illustrated in Fig. 9, where it is observed that the optimal average dimension $\langle s \rangle$ is, depending on the composition, around 100 μm to 200 μm, where the total power loss attains a minimum value (12). This is understood in terms of the opposite dependencies on grain size exhibited by the hysteresis loss component W_h, decreasing as $\langle s \rangle^{-n}$, with $n = 0.5$ to 1, and by the excess loss W_{exc}, approximately increasing as $\langle s \rangle^{1/2}$. A low-impurity content is mandatory in order to achieve this optimal grain size, because precipitates tend to hinder grain growth. In addition, some particles, like MnS and AlN, favor the establishment of a detrimental texture, rich of {111} planes. On the other hand, there are soluted impurities, like Sb and Sn, that can induce selective growth of those recrystallized grains having orientations close to the ideal random cubic texture {100}$\langle 0vw \rangle$. A similar texture can be approached, in two-stage reduced alloys, by increasing the Al concentration, up to 1.1 wt% (13) or even 1.8 wt% (14), which permits one to achieve $W_{15/50} \sim 2$ W/kg. The troublesome aspect of an increased Al content is, besides the cost, an increased tendency to surface and subsurface oxidation, occurring especially during the wet H_2 decarburization. In this case it is expedient to achieve the desired nonaging properties by decarburization and denitrogenization of the melt through vacuum degassing. The punching operation generates localized
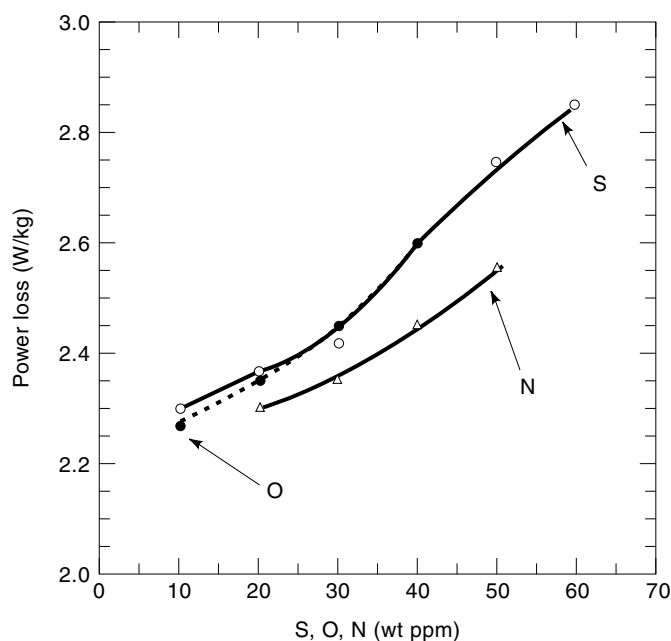

Figure 8. Influence of O, N, and S content on the power losss at 50 Hz and 1.5 T, in 0.35-mm-thick NO Fe–Si laminations. (Data taken from Ref. 12.)
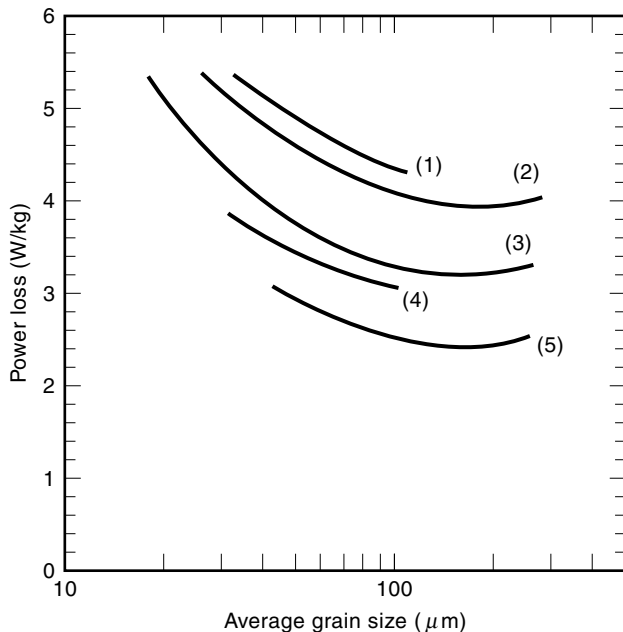
Figure 9. Power loss at 50 Hz and 1.5 T as a function of the average grain size in NO Fe–Si laminations, 0.50 mm thick. The curves (1) to (5) refer to materials having different (Si + Al) concentrations: (1) Si 0.01 wt%; (2) Si 0.3 wt%; (3) Si 0.8 wt% + Al 0.2 wt%; (4) Si 1.1 wt% + Al 0.2 wt%; (5) Si 3 wt% + Al 1 wt%. (Data taken from Ref. 14.)

internal stresses and, consequently, it might affect the loss figure in fully processed materials, where, in general, stress relief annealing is not performed. In large machines, however, a much larger effect on magnetic losses is expected to derive from the stresses permanently introduced by stacking and assembling the laminations in the core.

Grain-Oriented Silicon Steels

Fe single crystals exhibit minimum coercivity and maximum permeability when magnetized along one of the $\langle 001 \rangle$ axes. This property has fundamental implications on a theoretical level and has outstanding practical consequences. In fact, most transformer cores are built today with grain-oriented (GO) Fe–Si laminations, where the crystallites have their [001] easy axis close to the rolling direction (RD) and their (110) plane nearly parallel to the lamination surface. This is the so-called (110)[001] texture or Goss texture, after N. P. Goss, the first to develop such materials (3). The remarkable texture of GO alloys, together with a large grain size (from a few millimeters to a few centimeters) and a low content of impurities, lead to coercive fields as low as 4 A/m to 10 A/m and a maximum permeability around 5×10^4. These figures differ (by about an order of magnitude) from those typically found in NO alloys (see Fig. 1). Single-phase transformer cores can be made either by rolling up a long lamination or by stacking and suitably joining at the corners separate sheet pieces, so that the magnetic-flux path is everywhere aligned to RD. Three-phase cores are always of the stacked type and cover the high power range (starting from some 50 kVA). GO laminations are subdivided in two main classes: conventional grain-oriented (CGO) and high-permeability grain-oriented (HGO) alloys, characterized by a dispersion of the [001] axes

of the crystallites around RD of the order of ~7° and ~3°, respectively. The CGO materials, although less performing than the HGO ones, cover about 80% of the market. As illustrated in Table 3, commercial products are offered with thicknesses ranging between 0.35 mm and 0.23 mm and a loss figure $W_{17/50} = 1.40 - 0.80$ W/kg at 1.7 T and 50 Hz. More than 1 million ton/year of GO alloys are produced worldwide, with a market value estimated around US$3 billion. Following the original method by Goss, a number of patented processes for the production of GO sheets have been developed, based on various complex thermomechanical sequences (15–17). In the case of CGO materials, the main processing steps can be summarized as follows: (1) Melting in the arc furnace, vacuum degassing, and continuous casting. Besides Si, ranging in concentration between 2.9 wt% and 3.2 wt%, the following impurities are usually present: Mn (0.04 wt% to 0.1 wt%), S (0.02 wt%), C (0.03 wt%). (2) Slab reheating at 1300°C to 1350°C, followed by hot rolling to the thickness of 2 mm, annealing at a temperature of 900°C to 1100°C and rapid cooling. Times and temperatures along this stage are finely adjusted, in order to achieve a homogeneous distribution of precipitates, namely MnS particles with size around 10 nm to 20 nm. (3) Two-stage cold-rolling (~70% plus ~55%) to final gauge, with intervening annealing treatment at 800° to 1000°C. (4) Decarburizing anneal in wet H_2 atmosphere at 800° to 850°C. Since a huge amount of deformation is cumulated by the previous cold reduction, complete primary recrystallization takes place at this stage. However, the newly formed grains are strongly inhibited in their growth because of the presence of the finely precipitated MnS impurities. (5) MgO coating, coiling and 48 h box-annealing at a temperature of 1200°C. During this final annealing treatment, secondary recrystallization takes place, where abnormally large and sharply (110)[[001] oriented grains grow within the precipitate stabilized primary matrix and eventually cover the whole sheet. This is thought to occur because these grains have a boundary mobility much larger than the great majority of the primary grains, whose prevalent texture is around $\{111\}\langle 110 \rangle$ and $\{111\}\langle 112 \rangle$. It is estimated that one in about 10^6 primary grains is (110)[001] oriented, which explains the final large secondary-grain size. At the end of box-annealing the precipitates are completely dissolved and harmful effects on the magnetization process are avoided. (6) Phosphate coating and thermal flattening. The HGO laminations are obtained with some variants to the previous sequence, leading to a sharper Goss texture. Three basic industrial HGO processes are em-

Table 3. Typical Specifications for Conventional and High-Permeability Grain-Oriented Fe–(3 wt%)Si Alloys

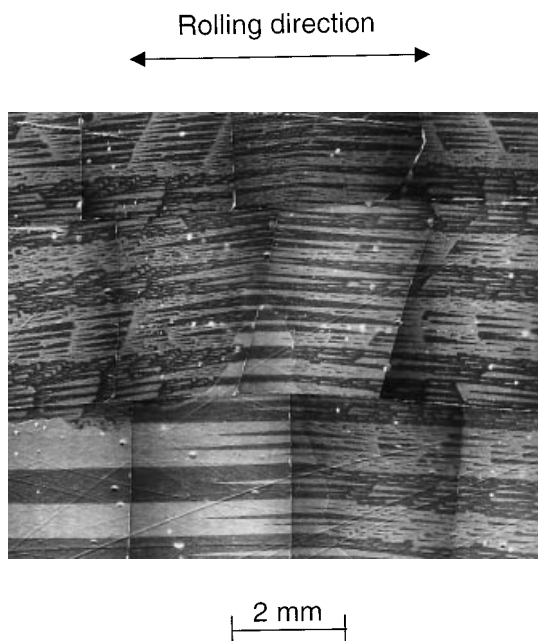| Alloy	Thickness (mm)	Specific Power Losses $B_p = 1.7$ T, $f = 50$ Hz (W/kg)	Induction at 800 A/m (T)
Conventional (CGO)	0.35	1.40	1.82
	0.30	1.30	1.83
	0.27	1.21	1.84
	0.23	1.15	1.84
High-permeability (HGO)	0.30	1.06	1.91
	0.27	0.99	1.92
	0.23	0.92	1.92
	0.23 (scribed)	0.80	1.90

Rolling direction

├─ 2 mm ─┤

Figure 10. Domain structure in an HGO Fe-(3 wt%)Si lamination. The main antiparallel domains are directed in each grain along the [001] axis. The supplementary flux-closing domains are formed when this axis is disoriented by more than ~1° with respect to the lamination surface.

ployed today. In a first process, where a single-stage 87% cold reduction is adopted, the MnS inhibitors are reinforced with AlN precipitates (15). A partial austenitic transformation during hot rolling, required for achieving AlN particles with optimal size, is obtained by adjusting the C concentration around 700 ppm. The second method is a two-step cold-rolling process which exploits the combined inhibiting action of MnSe precipitates and Sb solute atoms, segregated at grain boundaries (16). In the third process, solute B, N, and S atoms act as inhibitors and a single-stage cold reduction is again performed (17).

The beneficial effects on permeability and coercivity produced by an improved Goss texture are directly related to the morphology of the magnetic domains, which, for a perfect (110)[001] grain, form a bar-like array, with the 180° Bloch walls running along the [001] direction. This ideal structure is approached in the HGO sheets, which exhibit the lowest coercivity and the highest permeability among the Fe–Si alloys, thanks to the combined absence of DW pinning centers and presence of large well-oriented grains. Figure 10 shows a typical domain structure in an HGO lamination. One can notice that spike-shaped supplementary domains are present at the grain boundaries and at the surface of those grains having their [001] axis misoriented with respect to the lamination surface. Through these secondary domains, the magnetic flux can follow closed paths over short distances, which reduces the magnetostatic energy of the system. In a material with few, wide bar-like domains, like the one of Fig. 10, the magnetization reversal, localized at each instant of time at the moving walls, is highly nonhomogeneous and the excess loss component W_{exc} is accordingly large [see Eq. (3)]. In HGO materials with a sharp (110)[001] texture, this feature has detrimental consequences on power losses, because the excess

loss increase may wipe out the beneficial effects on permeability and dc coercivity introduced by the excellent texture. In order to optimize the material behavior both in terms of permeability and losses, it is common to apply, both in CGO and HGO laminations, a coating (thickness ~2.5 μm) capable of exerting a tensile stress of 2 MPa to 10 Mpa. This stress leads, via magnetoelastic interaction, to partial or complete disappearence of the flux closing domains, which have a high magnetoelastic energy cost. Under these conditions, the system reduces its magnetostatic energy by reducing the size of the main bar-like domains, ending into a more homogeneous magnetization process and reduced dynamic losses. However, the energy balance is such that stress-induced domain refinement hardly occurs when the grain misorientation angle $\beta < \sim 1.5°$. For this reason, in the best HGO materials, significant domain multiplication is achieved, through a combination of magnetoelastic and magnetostatic effects, by scribing patterns on the lamination surface. An array of scribing techniques (e.g., mechanical scratching, laser irradiation, plasma jet scribing, etch pitting) have been devised and are employed in the production of the highest HGO grades. The joint effects of tensile stress and surface scribing on power losses can be appreciated by experiments carried out in single crystals characterized by different values of the angle β (18). As shown in Fig. 11, the 50 Hz power loss is drastically reduced by scribing when $\beta < \sim 1°$, and further benefit is introduced by the tensile stress. This occurs with little detrimental
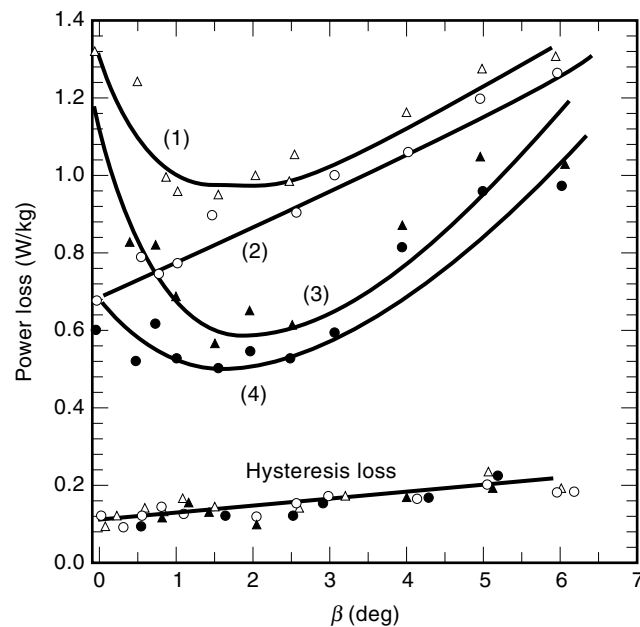

Figure 11. Power loss $P_{17/50}$ measured at 50 Hz and 1.7 T on 0.20 mm thick Fe–(3 wt%)Si single-crystal strips, as a function of the misorientation angle β made by the [001] direction with respect to the strip plane. Different tensile stresses and scribing conditions are considered: (1) $\sigma = 0$, before scribing; (2) $\sigma = 0$, scribed; (3) $\sigma = 15$ MPa, before scribing; (4) $\sigma = 15$ MPa, scribed. The application of the tensile stress σ and scribing of the strip surface bring about a definite decrease of $P_{17/50}$. The observed behavior of the dc hysteresis loss shows that this decrease is to be attribute almost completely to a corresponding decrease of the excess loss component. Combination of texture perfection with scribing permits one to achieve both maximum permeabilities and minimum losses.

effect on permeability (see Table 3). According to Eqs. (2) and (3), also a reduction of the lamination thickness would be, in principle, appropriate to improve loss figures. However, this may pose serious difficulties in controlling the processing parameters. At present, the lowest thickness of industrially prepared HGO laminations is 0.18 mm. These products show a loss value $W_{17/50}$ approximately 10% lower than the corresponding 0.23 mm thick HGO alloys, with a slight decrease of permeability. For applications at medium frequencies (400 Hz to 10 kHz), thinned GO laminations are commercially available, which are produced by rolling standard laminations to a reduced gauge of 0.15 mm to 0.10 mm and then carrying out an appropriate heat treatment. Because these alloys present relatively inferior texture and permeability, new processes have been devised in the laboratory in order to achieve highly oriented extra-thin materials. Excellent performances have been obtained in laminations with thickness from 10 μm to 100 μm by adopting, after cold reduction to the final gauge, a sequence of annealing treatments which induce a sharply defined (110)[001] texture through a tertiary recrystallization process (19) which occurs because the (110) crystallographic planes are those having minimum energy when exposed to the lamination surface. This principle is also at the basis of the preparation of cube-on-face (100)[001] textured Fe–(3 wt%)Si laminations by secondary recrystallization (20). These materials are, in principle, attractive because the biaxial symmetry introduced by two easy axes in the lamination plane has a potential for applications both in transformers and rotating machines. However, they have failed to attract commercial interest and their production has been discontinued.

Fe–(6.5 wt%)Si, Fe–Al and Fe–Si–Al Alloys

Fe–(6.5 wt%)Si alloys represent a prospective route to low-loss materials. When compared with the conventional Fe–(3 wt%)Si alloys, they exhibit a favorable combination of lower anisotropy ($K = 2.1 \times 10^4$ J/m^3 instead of ($K = 3.6 \times 10^4$ J/m^3) and increased resistivity ($\rho = 80 \times 10^{-8}$ $\Omega \cdot$m instead of $\rho = 45 \times 10^{-8}$ $\Omega \cdot$m), which compound with vanishing magnetostriction ($\lambda_{100} = -0.5 \times 10^{-6}$, $\lambda_{111} = 2 \times 10^{-6}$) to provide a potentially excellent soft magnetic alloy for applications at power and medium frequencies. Fe–(6.5 wt%)Si alloys cannot be prepared by cold-rolling because the heterogeneous formation of ordered FeSi (B_2) and Fe$_3$Si (DO$_3$) phases during cooling makes them hard and brittle. To avoid ordering, cooling rates greater than about 10^3 °C/s in the temperature interval 800° to 500°C are needed, a condition that can be satisfied by rapid quenching from the melt. By planar flow casting (PFC), a method where a molten metal stream is ejected onto a rotating metallic drum, ductile Fe–(6.5 wt%)Si ribbons are obtained, with thickness typically ranging between 30 μm and 100 μm. Once annealed in vacuum at 1100° to 1200°C, they exhibit a columnar grain structure ($\langle s \rangle \sim$ 100 μm to 500 μm) with a prevalent texture (100)$\langle 0vw \rangle$ (random cube-on-face). The final ribbons may show, at the price of a somewhat reduced ductility, a coercivity lower than 10 A/m and a maximum relative permeability larger than 10^4 and constant up to the kilohertz region. At 1 kHz and 1 T, the power loss can be lower than 15 W/kg in 50 μm thick ribbons, a value that favorably compares with the typical loss figure of thinned GO Fe–(3 wt%)Si laminations. Fe–(6.5 wt%)Si alloys can equally be prepared by Si enrichment of standard NO and GO lami-

nations. Classically, Si enrichment is carried out by means of a chemical vapor deposition (CVD) process, where SiCl$_4$ is used as the donor phase, according to the reaction SiCl$_4$ + 5Fe $\Leftrightarrow$ Fe$_3$Si + 2FeCl$_2$. This process has been industrially applied to NO laminations, prepared with thickness ranging between 0.10 mm and 0.30 mm (21). Materials with good workability are obtained, and the laminations can be bent and punched. For peak induction values below 1 T and frequencies higher than a few hundred hertz, the reported loss figures are better than those found in GO laminations of the same thickness. At the same time, the reduced magnetostriction yields a definite decrease of the acoustic noise level under operating conditions.

Solute Al and Si atoms affect in a similar way the physical properties of Fe (22), but Si is preferred in magnetic alloys because Al has a much higher tendency to react with oxygen and gather impurities, besides adding to the cost of the material. On the other hand, Fe–Al alloys are ductile, even when partial ordering occurs (above 7 wt% to 8 wt% Al concentration). The magnetostriction constant λ_{100} suffers an approximately fivefold increase on increasing Al up to 10 wt% (from 20×10^{-6} to $\sim$90 $\times 10^{-6}$), and it eventually drops around zero for Al concentrations of $\sim$16 wt%. At the same time, the anisotropy constant follows a monotonic decrease and, depending on the degree of ordering, passes through zero around 11 wt% to 14 wt% Al. Two compositions have applicative relevance. The Fe–(13 wt%)Al alloy combines high magnetostriction with low anisotropy and is of interest for magnetoelastic transducers. The Fe–(17 wt%)Al alloy is characterized by mechanical hardness and high permeability and is used in magnetic heads. The ternary Fe–(9.6 wt%)Si–(5.5 wt%)Al alloy, known as Sendust, is characterized by an extremely soft magnetic behavior, because the constants K_1, λ_{100}, and λ_{111} all simultaneously approach the zero value. The coercive field can reach values around 1 A/m to 2 A/m, and the relative permeability is of the order of 10^5. Sendust alloys are extremely brittle and are therefore used in cast form for dc applications and as powder cores in ac devices.

AMORPHOUS AND NANOCRYSTALLINE ALLOYS

Amorphous soft magnetic materials can be obtained as thin laminations by means of rapid solidification. Today, the predominantly employed rapid solidification technique is planar flow casting (PFC), by which one can prepare ribbons of variable width (up to 100 mm or 200 mm) and thickness usually ranging between 10 μm and 50 μm. In a typical PFC setup, a quartz crucible, which holds the liquefied master alloy, is placed nearly in contact with the surface of a rotating metallic drum, which drags the liquid at a velocity of 10 m/s to 40 m/s. This ensures a cooling rate of the order of 10^5°C/s to 10^6 °C/s, sufficient to undercool the alloy through the glass transition temperature T_g, where it achieves the typical viscosity of a solid, retaining, at the same time, the disordered atomic arrangement typical of a liquid. Amorphous alloys can also be produced as wires of 50 μm to 100 μm diameter by the so-called in-water-quenching technique, where the molten metal jet is plunged into rotating water (23). The general composition of soft magnetic amorphous alloys is $T_{70-80}M_{30-20}$, where T stands for one or more of the transition metals Fe, Co, and Ni, and M is a combination of metalloids (e.g. B, Si, P, C). The

metalloid atoms, with their radius much smaller than that of Fe, Co, and Ni, play an indispensable role as glass formers, besides providing the eutectic composition required for the safe achievement of the amorphous state. Lack of crystalline order does not prevent the formation of ferromagnetic order. The existence of a large-scale magnetic moment is basically unaffected by disorder, although its strength is reduced by the presence of the metalloids (24). The Ni atoms do not apparently contribute to the total magnetic moment, so that it is usual to classify magnetic glasses simply as Fe-based or Co-based. The Curie temperature T_c of an amorphous alloy is found to be lower than that of the corresponding crystalline alloy, with the remarkable property that in the Fe-based materials it decreases when the proportion of Fe is increased, pointing to an extrapolated minimum T_c value for hypothetical pure amorphous Fe. Figure 12 shows that the saturation magnetization decreases by a noticeable amount when passing from the Fe-rich to the Co-rich composition in the representative alloy $Fe_{80-x}Co_xB_{20}$ (24). The mean free path of conduction electrons in glassy metals is of the order of the interatomic distance, and the electrical resistivity is consequently increased by a factor 2 to 3 with respect to their crystalline counterpart and is quite independent of temperature. At the same time, plastic slip is highly limited, because no dislocation glide is possible and a very high fracture stress $\sigma_r \sim 2800$ MPa is obtained, with cumulated strain around 2.5%. The ratio E/σ_r, where E is the Young's modulus, attains a value ~50, which is typical of high-strength materials and makes amorphous alloys interesting for structural applications. As summarized by the parameters presented in Table 4, the disordered atomic structure provides a unique combination of mechanical hardness and magnetic softness, the latter coming from a subtle mechanism which involves the competition between the exchange interaction responsible for ferromagnetic order and the local anisotropies. One may describe an amorphous alloy as a random ensemble of structural units, each extending over a distance δ equal to few atomic spacings, that have definite symmetry properties and are therefore characterized by a local magnetocrystalline anisotropy of strength K, oriented at random. In 3d-based alloys, where K is of the order of 10^4 J/m³ to 10^5 J/m³, the anisotropy strength is not large enough to force the local alignment of the magnetization to the easy axis of the individual structural units. Because of the exchange interaction, the magnetization maintains the same orientation over a correlation length $L \gg \delta$. The effective magnetocrystalline anisotropy of the material results from the average of the local anisotropies over distances of the order of L, which leads to a very low final value K_{eff}, according to the equation

$$K_{eff} \approx \frac{K^4\delta^6}{A^3} = K\left(\frac{\delta}{L}\right)^6 \qquad (4)$$

where the constant A measures the strength of exchange interactions and $L = \sqrt{A/K}$ (6). For a structural wavelength $\delta \approx 10^{-9}$ m and a value $A \approx 10^{-11}$ J/m we can estimate an effective anisotropy $K_{eff} \approx 10^{-6}$ J/m to 10^{-1} J/m³, depending on the value of K. This negligible value of the average magnetocrystalline anisotropy is the key to the soft magnetic properties of the amorphous alloys. In fact, under these conditions, coercivity and permeability are due only to residual anisotropies of magnetoelastic origin, or to induced anisotropies created by suitable treatments. A stress of intensity σ causes a uniaxial anisotropy $K_\sigma = \frac{3}{2}\lambda_s\sigma$ in a material characterized by the saturation magnetostriction constant λ_s. This value provides a sort of a priori indicator of the achievable ultimate soft magnetic properties of a given amorphous alloy. Figure 12 shows that in the composition $Fe_{80-x}Co_xB_{20}$ λ_s strongly depends on the relative proportions of Fe and Co, ranging from positive to negative values (from ~30 × 10⁻⁶ to ~−3 × 10⁻⁶)
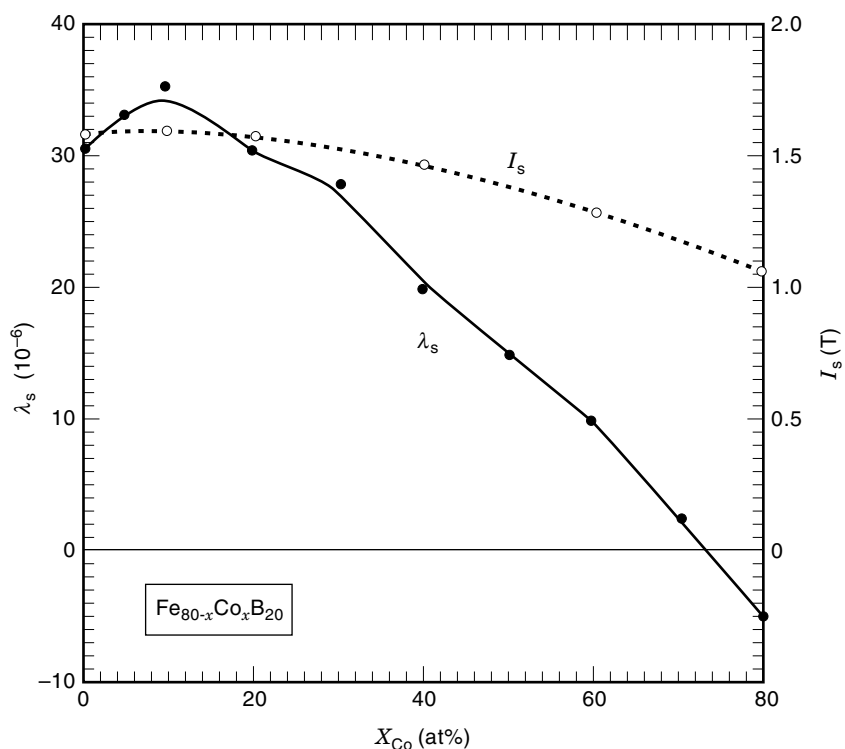

Figure 12. Evolution of saturation magnetization I_s and magnetostriction constant λ_s with the concentration x of Co atoms in $Fe_{80-x}Co_xB_{20}$ amorphous alloys. Zero magnetostriction is achieved around $x = 75$ at%.

Table 4. Physical and Magnetic Properties of $Fe_{78}B_{13}Si_9$ Amorphous Alloys Compared with Those of Grain-Oriented Fe-(3 wt%)Si Laminations

Property	Amorphous Ribbon $Fe_{78}B_{13}Si_9$ (thickness 0.025 mm)	GO Fe–(3 wt%)Si (thickness 0.23 mm)
Density (kg/m^3)	7.2×10^3	7.65×10^3
Young's modulus (GPa)	150	120
Yield stress (MPa)	700	300
Fracture stress (MPa)	2800	350
Fracture strain (%)	2.5	25
Vicker's hardness	800	180
Electrical resistivity ($\Omega \cdot$ m)	135×10^{-8}	45×10^{-8}
Lamination factor (%)	<90	95
Curie temperature (°C)	410	740
Saturation polarization (T)	1.55	2.03
Saturation magnetostriction	36×10^{-6}	25×10^{-6} (λ_{100})
dc coercive field (A/m)	2 (after annealing)	5
Max relative permeability	2×10^5 (after annealing)	8×10^4
50 Hz power loss at 1.4 T (W/kg)	0.25 (after annealing)	0.60

on passing from the Fe-rich to the Co-rich side, and intersecting the value $\lambda_s \sim 0$ at Fe concentrations around 5 at% to 8 at%. In the highly magnetostrictive Fe-rich alloys, the random distribution of internal stresses introduced during the rapid solidification, typically of the order of 50 MPa to 100 MPa, controls coercivity through the formation of complex anisotropy patterns, with K values in the range of some 10^3 J/m^3 (25). These stresses can never be completely relieved by annealing, because the treatment temperatures are in any case limited by the necessity to avoid the slightest precipitation of crystalline phases. Even after carefully controlled annealing under a saturating longitudinal field, the Fe-based ribbons reach at best coercive fields of 2 A/m to 3 A/m. The influence of stress anisotropies becomes negligible in the Co-rich alloys with vanishing magnetostriction. Accordingly, these materials exhibit the lowest energy losses and the highest permeability at all frequencies. In addition, their properties can be tuned to specific needs by suitable thermal treatments under a saturating magnetic field, which induce a large-scale anisotropy K_u as a consequence of localized atomic rearrangements having a definite directional order. Being the only form of anisotropy present in the material, K_u fully governs coercivity, permeability, and loop shapes. Figure 2 provides an example of the magnetic softness and versatility of the near-zero-magnetostrictive Co-based alloys, which, prepared as very thin ribbons (8 μm to 15 μm), favorably compete with ferrite and Fe–Ni cores up to the MHz region, where they can display initial relative permeabilities approaching 10^4 (26). The extra-soft magnetic properties of the Co-rich compositions are obtained at the expenses of a substantial reduction of the saturation magnetization with respect to the Fe-based alloys (0.9 T to 0.5 T versus 1.3 T to 1.6 T). This compounds with the obvious cost problems related to the use of Co, so that the related alloys are reserved for specialized applications. Amorphous wires prepared by the in-water-quenching technique exhibit a bistable magnetic behavior, regardless of the sign of the magnetostriction. This property derives from the special domain structure that is formed in the wire, typically made of an active longitudinal core, reversing its magnetization with a single Barkhausen jump, and an outer shell, having radial or circumferential domains. The origin of such a structure is to be found in the anisotropies induced by the large stresses frozen-in during the solidification process, in association with the anisotropy of magnetostatic origin (shape anisotropy). The switching-like behavior of the magnetization reversal in amorphous wires can be exploited in a number of applications, like jitter-free pulse generators, digitizing tablets, speed and position sensors, and anti-theft devices.

Table 5 summarizes the behavior of the main physical parameters in a number of common amorphous alloys. Fe-based alloys are the materials of choice in applications like distribution transformer cores, where they can often replace the high permeability GO Fe–Si laminations. Figure 13 shows that a

Table 5. Physical Parameters in Representative Amorphous Alloys

Alloy	I_s (T)	T_c (°C)	T_x (°C)	ρ (10^{-8} $\Omega \cdot$ m)	λ_s (10^{-6})	H_c (A/m)
$Fe_{80}B_{20}$	1.60	375	450	122	32	3
$Fe_{78}B_{13}Si_9$	1.56	415	550	137	27	2.4
$Fe_{81}B_{13.5}Si_{3.5}C_2$	1.61	370	480	135	30	3.2
$Co_{80}B_{10}Si_{10}$	0.90	520	410	108	−4	7
$Co_{71}Fe_4B_{15}Si_{10}$	0.87	352	520	124	−0.2	0.4
$(Co,Fe)_{70}(Mo,Si,B)_{30}$	0.55	250	500	130	−0.2	0.4

$I_s \equiv$ saturation magnetization; $T_c \equiv$ Curie temperature; $T_x \equiv$ crystallization temperature; $\rho \equiv$ electrical resistivity; $\lambda_s \equiv$ saturation magnetostriction constant; $H_c \equiv$ coercive field. The data refer to materials treated in order to provide best performances.
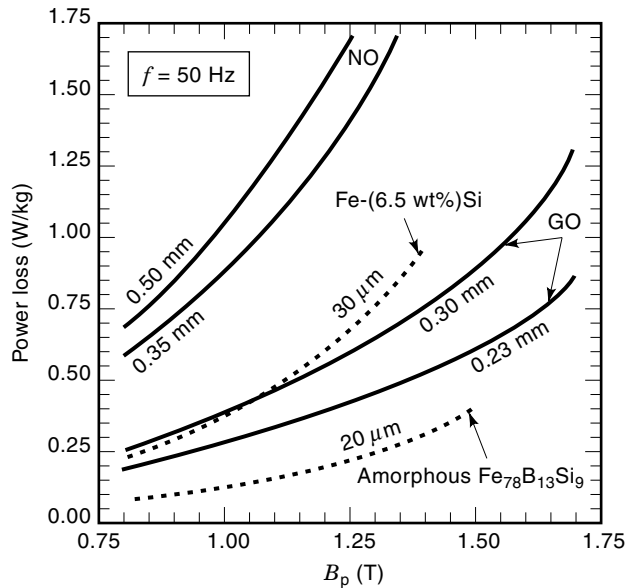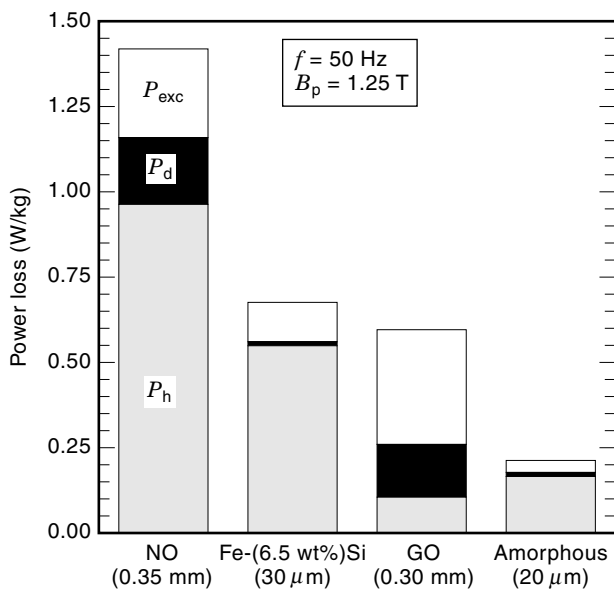
Figure 13. Total power loss at 50 Hz versus peak induction B_p (a), and loss decomposition at $B_p = 1.25$ T (b), in the following soft magnetic alloys: NO Fe–(3 wt%)Si laminations, 0.35 mm and 0.50 mm thick; Fe–(6.5 wt%)Si rapidly quenched ribbons, 30 μm thick; GO Fe–(3wt%)Si laminations, 0.30 mm and 0.23 mm; $Fe_{78}B_{13}Si_9$ amorphous ribbons, 20 μm thick. The excess loss component P_{exc} is the largest one in the GO laminations, whereas the classical component P_{cl} is negligibly small in the high Si and amorphous ribbons.

significant loss reduction can be obtained at 50 Hz on passing from GO to amorphous $Fe_{78}B_{13}Si_9$ laminations. The loss analysis, schematically illustrated in Fig. 13(b), demonstrates that this is due to a drastic reduction of the excess and the classical loss components, brought about, according to Eqs. (2) and (3), by the combination of low ribbon thickness and high material resistivity. In recent years, increasing emphasis on en-

ergy saving has favored the introduction by electrical utilities of distribution transformers made of amorphous alloy cores, especially in the single-phase low power range (10 kVA to 50 kVA). These devices are characterized by reduced total ownership costs, regarding both purchasing and operating costs along the device lifetime, besides exhibiting good stability over time (27). Less favorable economic conditions are attached to applications in three-phase power transformers. Significant use of amorphous alloys is made in electronics (28). For instance, Co-based alloys are ideal as cores of inductive components to be employed up to frequencies of the order of 1 MHz, as found, for instance, in the switched-mode power supplies and in digital telecommunication circuits. Their low I_s value is not a disadvantage in these cases, where, in order to limit core heating, the working induction is always kept small. The unique combination of high elastic limit and high magnetostriction in the Fe-based materials is exploited in high-sensitivity sensors and transducers. Further applications include electromagnetic interference filtering, magnetic heads, various types of magnetic shielding, and ground fault interrupters.

Amorphous alloys tend to crystallize heterogeneously upon annealing, with scattered nucleation and growth of microcrystals taking place at temperatures well below the bulk transition to the crystalline state. This has detrimental consequences on the soft magnetic behavior of the material, besides being associated with drastic mechanical embrittlement. Fe-based alloys do need stress-relief annealing in order to achieve optimized magnetic properties, but if the treatment temperature is brought to values of the order of 400°C, a sharp increase of the coercive field is observed, due to the heterogeneous formation of microcrystals of 0.1 μm to 1 μm size (29). In Fe–Si–B alloys, however, it is possible to achieve both homogeneous accelerated grain nucleation and restrained grain coarsening by the addition of Cu and Nb (30). In particular, by subjecting amorphous ribbons with composition $Fe_{73.5}Cu_1Nb_3B_9Si_{13.5}$ to annealing at a temperature around 550°C, a homogeneous nanocrystalline structure is obtained, composed of α-Fe–($\sim$20 at%)Si grains, having dimensions of the order of 10 nm, embedded in a residual amorphous matrix. The crystallites occupy about 70% of the material volume and are separated by amorphous layers 1 nm to 2 nm thick. Quite a similar structure can be obtained in alloys with composition $Fe_{91-84}(Zr, Nb)_7B_{2-9}$, with the crystalline phase now being made of α-Fe grains (31). Since the grain size δ is smaller than the correlation length $L = \sqrt{A/K}$ and the intervening amorphous phase ensures grain-to-grain exchange coupling, vanishing crystalline anisotropy is obtained. In particular, with $\delta = 10$ nm, $K = 10^4$ J/m^3, and $L = 50$ nm, Eq. (4) yields a value of the average magnetocrystalline anisotropy constant $K_{eff} \sim 0.5$ J/m^3. This feature does not come alone, because also magnetostrictive anisotropies average out to vanishing values. In fact, there is a balance in the material between the negative magnetostriction of the crystalline phase and the positive magnetostriction of the amorphous phase. Any applied or residual stress may generate anisotropies at the nanometer scale, having directions dictated by the nature of the stress (tensile/compressive), its direction, and the sign of the magnetostriction constant, but, again, the exchange interaction acts to suppress any mesoscopic and macroscopic anisotropy. Equation (4) suggests that the coercive field, which can be roughly estimated to be proportional to the

average anisotropy constant K_{eff}, increases with the sixth power of the grain size δ. Experiments show that this relationship is verified to a good approximation up to $\delta \sim 100$ nm (32), a limit beyond which the coercive field starts decreasing with increasing δ. Fe-based nanocrystalline alloys emulate the properties of the amorphous Co-based alloys, with the advantage that one can deal with inexpensive raw materials while achieving higher saturation magnetization (e.g., 1.24 T in $Fe_{73.5}Cu_1Nb_3B_9Si_{13.5}$ and 1.63 T in $Fe_{91}Zr_7B_2$ versus 0.61 T in $Co_{67}Fe_4B_{14.5}Si_{14.5}$ and 0.86 T in $Co_{71}Fe_4B_{15}Si_{10}$) and improved thermal stability. The hysteresis loop of nanocrystalline alloys can be tailored to specific applications by means of induced anisotropies. In particular, linear, low-remanence hysteresis loops can be achieved by suitable treatments under transverse field which are characterized by low power losses and high permeabilities up to frequencies of several hundred kilohertz, as illustrated in Fig. 14.

NICKEL-IRON AND COBALT-IRON ALLOYS

Nickel–iron alloys have a special position in the landscape of soft magnetic materials, because of the broad range of properties they can display, both as a function of composition and in response to various kinds of treatment. These properties can be exploited in practice because there are no restraints to cold working and it is possible to roll laminations with good precision, down to very low thickness (10 μm to 20 μm). The versatility of Ni–Fe is already apparent from the dependence of its intrinsic magnetic parameters on the relative proportions of the two constituent elements, summarized in Fig. 15. It can be noticed that both the first magnetocrystalline anisotropy constant K_1 and the magnetostriction constants λ_{100} and λ_{111} pass through zero in the Ni-rich side, with a positive K_1 value (i.e., a $\langle 100 \rangle$ easy axis) coexisting with a γ (fcc) structure up to ~ 75 wt% Ni. The evolution of K_1 with the Ni concentration is strongly related to the extent of structural ordering introduced by the formation of the Ni_3Fe phase. The ordering reaction, which occurs below 500°C, is rather sluggish and can be controlled to a good extent by the choice of the annealing temperature and the cooling rate. It can also be restrained by introduction of additives like Mo, Cu, and Cr. Compositions with Ni < 30 wt% are ill-defined from the structural point of view, and their magnetic properties bear little interest. The Fe70–Ni30 alloy is characterized by a singularity drop of the Curie temperature T_c, which becomes of the order of room temperature. T_c increases in a near-linear fashion in the range 30 wt% to 35 wt% Ni, a property that is sometimes exploited in magnetic shunt devices. At 36 wt% Ni T_c has already reached the value of 230°C, the thermal expansion coefficient is extremely low ($\sim 1 \times 10^{-6}$ K^{-1}, the so-called "Invar behavior"), and the resistivity is pretty high (75 $\times 10^{-8}$ $\Omega \cdot$m). This latter feature is conducive to low losses at high frequencies and makes the Fe64–Ni36 tapes interesting for applications like radar pulse transformers. The Fe50–Ni50 alloys, which are characterized by a high saturation magnetization I_s = 1.6 T, can be prepared as strongly (100)[001] textured sheets by means of severe cold rolling to the final thickness (>95%) and primary re-crystallization annealing at around 1000°C. The favorable directional feature provided by the texture can be reinforced by the anisotropy K_u induced by longitudinal magnetic annealing, made at a temperature around
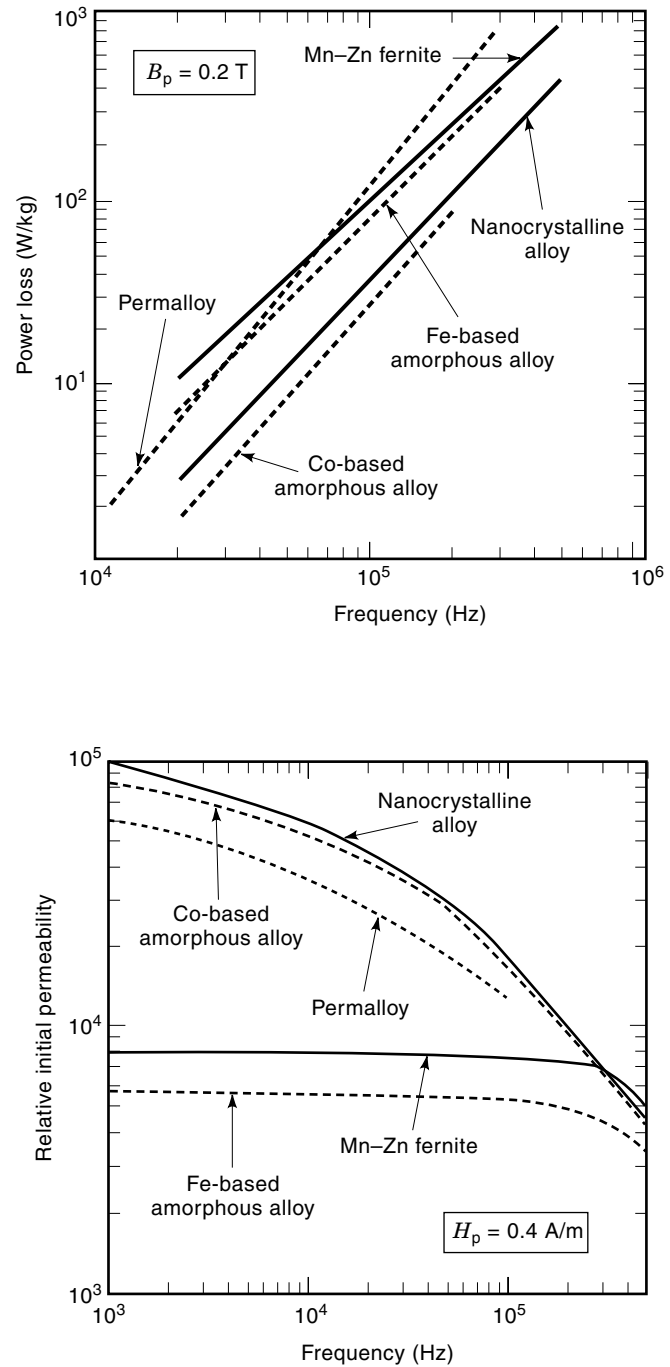

Figure 14. Frequency dependence of relative initial permeability (peak field H_p = 0.4 A/m) and power losses (peak induction B_p = 0.2 T) in nanocrystalline $Fe_{73.5}Cu_1Nb_3B_9Si_{13.5}$ ribbons, 18 μm thick. The samples have been field annealed, in order to have low-remanence and best high-frequency properties. Comparison is made with the behavior of Fe20–Ni80 (Permalloy) tapes and Fe-based and Co-based amorphous ribbons, having similar thickness and having been similarly field treated. The properties of typical Mn–Zn ferrites are also shown. (Data taken from Ref. 30.)
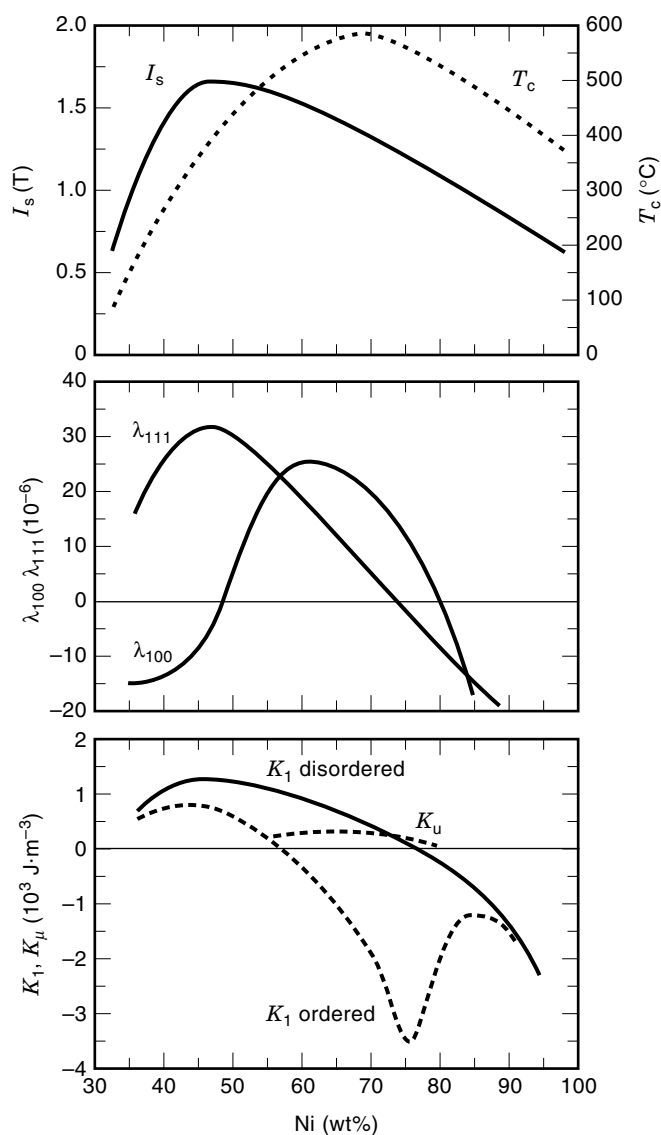
Figure 15. Dependence of the intrinsic magnetic parameters on the Ni concentration in Ni–Fe alloys. $I_s \equiv$ saturation polarization; $T_c \equiv$ Curie temperature; $K_1 \equiv$ magnetocrystalline anisotropy constant; $K_u \equiv$ anisotropy induced by field annealing; λ_{100} and $\lambda_{111} \equiv$ magnetostriction constants. T_c approaches room temperature for Ni $\sim$ 30 wt% and interesting magnetic properties are observed only at higher Ni concentrations. The anisotropy constant K_L depends, besides the composition, on the degree of structural ordering, associated with the formation of a Ni_3Fe phase, and is thereby related to the annealing temperature and the cooling rate.

or lower than 450°C ($T_c \sim$ 500°C) and followed by slow cooling. In this way a squared hysteresis loop is achieved, to be exploited, for instance, in magnetic amplifiers and saturable reactor cores. By increasing the Ni content toward 55 wt% to 60 wt%, the induced anisotropy K_u, which can reach the value of 300 J/m³ to 400 J/m³, becomes comparable with the magnetocrystalline anisotropy K_1. By annealing under a transverse saturating field, one can therefore achieve a sheared low-remanence hysteresis loop, characterized by a large unipolar swing (0.9 T to 1.2 T). This feature is welcome in devices like unipolar pulse transformers or ground fault interrupters. The highest permeabilities and lowest coercivities are obtained at around 75 wt% to 80 wt% Ni concentration, because it is possible to approach vanishing values for both magnetostriction and anisotropy. Figure 15 actually shows that it is not possible to simultaneously achieve zero values for K_1, λ_{100}, and λ_{111}. It is therefore expedient to make calibrated additions of elements like Mo, Cu, and Cr, by which one can achieve an isotropic magnetostriction constant $\lambda_s \sim 0$ and a better control of the Fe_3Ni phase ordering through annealing and cooling. Since the anisotropy constant K_1 depends on ordering, it is possible to devise a thermal treatment leading to $K_1 \sim 0$ (33). A further advantage introduced by the additional elements is a substantial increase of the resistivity (e.g., from 20×10^{-8} $\Omega \cdot$ m to 62×10^{-8} $\Omega \cdot$ m by introducing 5 wt% Mo in 78 wt% Ni alloys), at the cost of a certain reduction of I_s. As reported in Table 6, a coercive field lower than 1 A/m and a relative initial permeability higher that 10^5 can be obtained in these alloys, which are generally known under the commercial name of Permalloys. A typical dc hysteresis loop in a Permalloy tape is given in Fig. 16(a), illustrating through comparison with the loop of a GO Fe–Si lamination a somewhat extreme example of magnetic softness. By field annealing at temperatures ranging between 250°C and 380°C, a substantial change of the hysteresis loop of Permalloys can be obtained, because the magnetocrystalline anisotropy can be easily overcome by the anisotropy K_u induced through magnetic ordering (less than 100 J/m³). Figure 16(b) provides an example of loop shearing by transverse field annealing in these materials. It should be remarked that K_1 increases with decreasing temperature, and for applications occurring far from room temperature some variant to the standard treatment must be introduced. For instance, in order to develop Permalloys for cryogenic applications, the annealing temperature and the cooling rate are conveniently reduced, in order to shift the achievement of $K_1 \sim 0$ to such temperatures.

Cobalt–iron alloys do not display outstanding soft magnetic properties, but represent a unique solution in terms of Curie temperature and saturation magnetization, both remarkably higher than in pure Fe. In the classical Fe50–Co50

Table 6. Properties of Some Basic Fe–Ni and Fe–Co Alloys

	I_s (T)	T_c (°C)	ρ (10^{-8} $\Omega \cdot$ m)	H_c (A/m)	μ_i ($\times 10^3$)
Fe64–Ni36	1.30	230	75	40	2
Fe50–Ni50	1.60	490	45	7	15
Fe15–Ni80–Mo5	0.80	400	60	0.4	150
Fe14–Ni77–Mo4–Cu5	0.78	400	60	1.5	40
Fe49–Co49–V2	2.40	980	27	100	2

$I_s \equiv$ saturation polarization; $T_c \equiv$ Curie temperature; $\rho \equiv$ electrical resistivity; $H_c \equiv$ coercive field; $\mu_i \equiv$ relative initial permeability. Compositions are given in wt%.
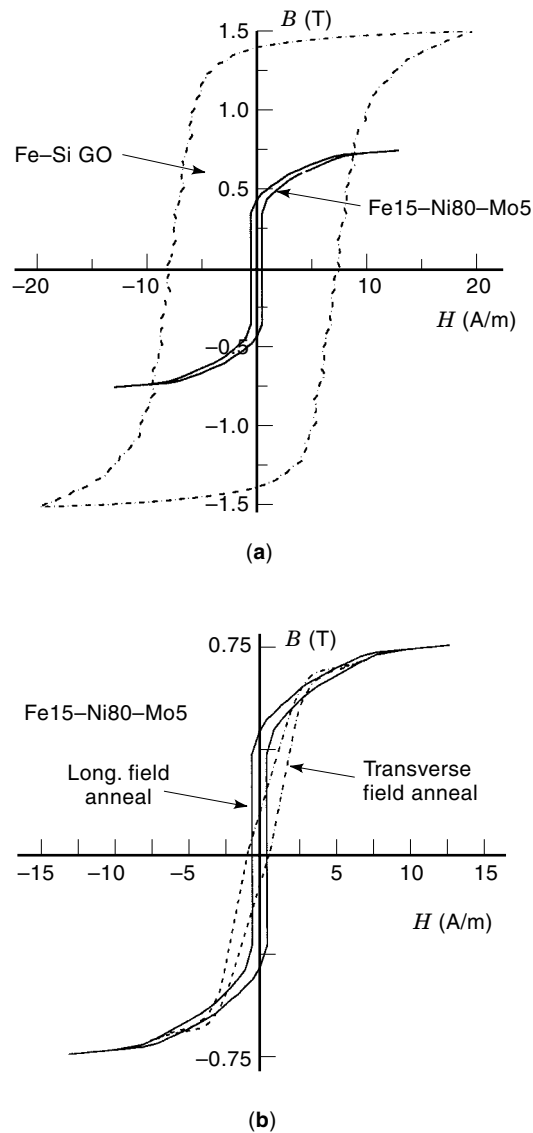
Figure 16. (a) Static hysteresis loops in a GO Fe–(3wt%)Si lamination and in an Fe15–Ni80-Mo5 (Permalloy) tape. (b) Effect on the Permalloy loop shape of annealing under a transverse saturating field.

alloy we have, for instance, $T_c = 980°C$ and $I_s = 2.40$ T, which proves useful for a number of applications, where volume reduction and high working temperature may be required. This may be the case of onboard high-speed generators for aircrafts and spacecrafts, where the cost of Co is of little concern. The Fe50–Co50 alloy transforms from fcc (γ) to bcc (α) solid solution at 1000°C and undergoes rapid long-range ordering below 730°C. The $\alpha–\gamma$ transformation can limit to some extent the recrystallization process and solid-state refining, while ordering detrimentally affects the mechanical properties, leading to a brittle material. Ordering can, however, be retarded by addition of 2 wt%V and rapid quenching, so that Fe49–Co49–V2 alloys can eventually be prepared as thin sheets by cold rolling, with the further benefit of a large increase of resistivity with respect to Fe50–Co50 (27 × 10^{-8} $\Omega \cdot$ m versus 7 × 10^{-8} $\Omega \cdot$ m.). By adjusting the cooling rate, one can also dramatically affect the anisotropy constant, which can be

made to approach the zero value, but the magnetostriction always remains extremely high, with $\lambda_{100} \sim 150 \times 10^{-6}$ and $\lambda_{111} \sim 30 \times 10^{-6}$. This ultimately hinders the achievement of a very soft magnetic behavior. The value of the coercive field in regular Fe49–Co49–V2 alloys (Permendur) is around 100 A/m, with a relative permeability of $\sim 2 \times 10^3$. A substantial property improvement can be obtained by very careful control of the material purity and magnetic field annealing. The high-purity alloy, called Supermendur can exhibit $H_c \sim 10$ A/m and $\mu \sim 8 \times 10^4$.

SOFT FERRITES

Soft spinel ferrites are the magnetic materials of choice for most applications at frequencies above the audio range, up to a few hundred megahertz, because of their nonmetallic character. They have the general composition $MO \cdot Fe_2O_3$, where M is a divalent metal ion such as Fe^{2+}, Mn^{2+}, Ni^{2+}, Zn^{2+}, Mg^{2+}. Typical applications include pulse and wide-band transformers for television and telecommunications, inductor cores in switched-mode power supplies, antenna rods, cores for electromagnetic interference suppression, and magnetic heads. For frequencies in the range 500 MHz to 500 GHz the so-called microwave ferrites have been developed. They are used in a variety of devices, such as waveguide isolators, gyrators, and modulators, to control the transmission or absorption of electromagnetic waves. Besides some types of spinel ferrites, hexagonal ferrites (like $BaFe_{12}O_{19}$) and garnets (like $Y_3Fe_5O_{12}$) are employed for this purpose. The magnetic properties of ferrites are due to the magnetic moments of the metal ions. The ion–ion interaction is antiferromagnetic in nature and leads to the distinctive temperature dependence of the magnetization shown in Fig. 17. The oxygen ions in spinel ferrites are arranged in a close-packed face-centered cubic structure and the small metal ions slip into interstitial positions, either at tetrahedral (A) or octahedral (B) sites, which are surrounded by four and six oxygen ions, respectively. In a unit cell, which contains eight formula units (i.e., 32 O^{2-} ions, 16 Fe^{3+} ions, and 8 M^{2+} ions), 8 of the available A sites and 16 of the available B sites are occupied by the metal ions. When the M^{2+} ions and the Fe^{3+} ions are in the A and B sites, respectively, we have the so-called *normal spinel* structure, whereas the *inverse spinel* structure is obtained when the 16 Fe^{3+} ions are equally subdivided between the A and B sites, the latter being shared with the M^{2+} ions. However, intermediate cases are very common. The spontaneous magnetization of ferrites and its temperature dependence were explained by Néel (35) by assuming that the spin moments of the metal ions in the A and B sublattices are antiferromagnetically coupled through indirect exchange interaction. Actually, since the cations are separated by the oxygen anions, direct exchange interaction between their 3d electron spins is negligible and an indirect coupling mechanism, the superexchange (36), is expected to take place. This involves the spins of the two extra 2p electrons in the O^{2-} ion, which interact by direct exchange with the 3d spins of two neighboring metal cations. The mediating effect of the oxygen spins is such that, if the two cations have more than five 3d electrons, as is the case for Fe^{2+}, Co^{2+}, and Ni^{2+}, their total magnetic moments are bound to antiparallel directions. The strength of the superexchange interaction is the greatest when a straight line con-
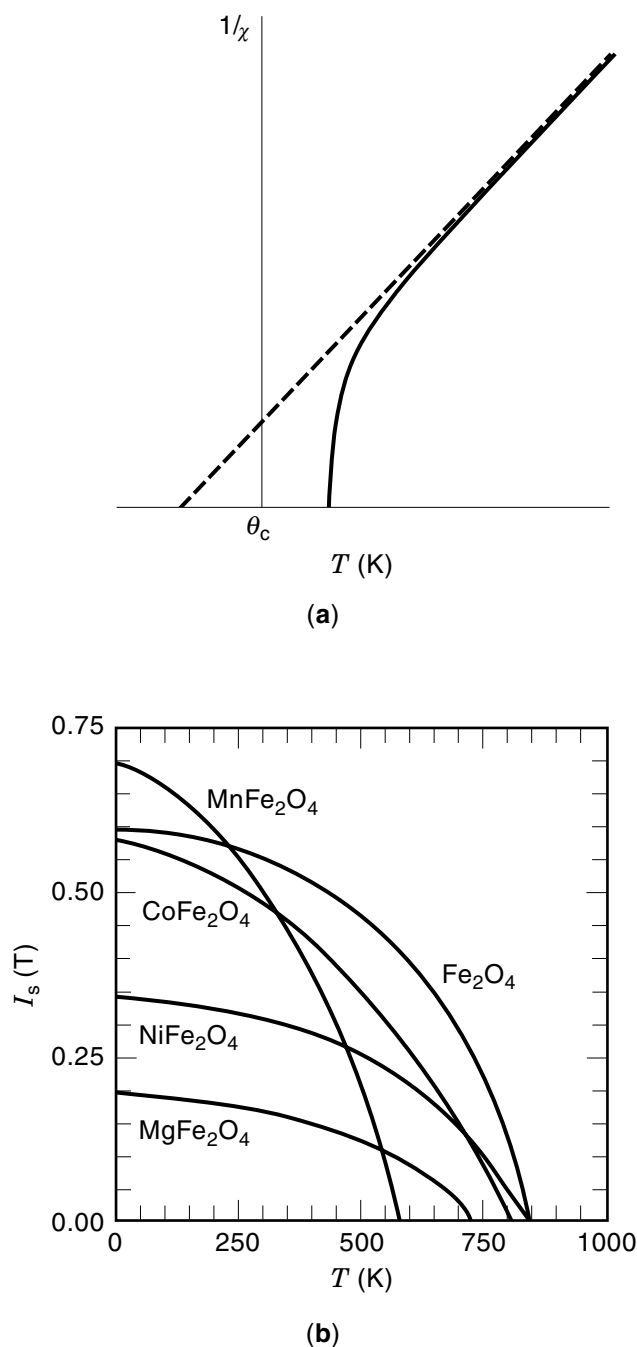
(a)

(b)

Figure 17. (a) Predicted temperature dependence of the inverse susceptibility in a ferrimagnetic material (35). (b) Saturation magnetization versus temperature in various cubic ferrites (34).

nects the cations through the O^{2+} ion. The A–B coupling, which is associated to an A–O–B angle around 125°, is then much stronger than the A–A and B–B couplings, where the angles are 90° and 80°, respectively. At the end, one is left with a system made of two coupled arrays of anti-parallel magnetic moments of unequal magnitude, which results in a net magnetic moment. This uncompensated antiferromagnetic behavior is called *ferrimagnetism* and the resulting magnetic moment per unit cell can be calculated through Néel's hypothesis. These calculations are in good agreement with the experimental values of the saturation magnetization

and are supported by neutron diffraction experiments. Although the magnetic moment per formula unit may be very large in terms of number of Bohr magnetons, the saturation magnetization I_s of spinel ferrites is low (typically around or below 0.5 T at room temperature), because of the low density of the uncompensated magnetic ions. In addition, the temperature dependence of I_s, which results from the composition of the temperature variations of the magnetization of the individual sublattices, may give rise, according to Néel's theory, to a variety of behaviors (37).

Most magnetic spinel ferrites, like $FeFe_2O_4$, $NiFe_2O_4$, $CoFe_2O_4$ are of the inverse type. In this case the magnetic moment per formula unit equals that of the M^{2+} ion, because the Fe^{3+} ions are evenly distributed over the A and B sublattices. The $ZnFe_2O_4$ ferrite is of the normal type, but, since the Zn^{2+} ion has a closed $3d$ shell and zero magnetic moment, it is paramagnetic at room temperature. $MnFe_2O_4$ is an example of partly normal and partly inverse spinel structure, where the Mn^{2+} and Fe^{3+} share in certain proportions the A and B sites. Table 7 provides a general overview of the properties of spinel ferrites. The differences observed between predicted and measured magnetic moments are ascribed to a number of factors, like imperfect quenching of the orbital magnetic moments, changes in the ion valence, and fluctuations in the cation distribution between the A and B sites. Such differences are small, in general, except for $CoFe_2O_4$, where the orbital contribution is important. Ferrites, being ionic compounds, are insulators in principle and display in practice a wide range of resistivity values, always orders of magnitude higher than in typical Fe–Si or amorphous alloys. The most important conduction mechanism is the transfer of electrons between Fe^{2+} and Fe^{3+} ions in the octahedral sites. Magnetite ($FeFe_2O_4$) therefore exhibits a nearly metallic behavior, with resistivity $\rho \sim 10^{-5}\ \Omega \cdot m$.

Most technical spinel ferrites are of the mixed type, where the presence of two or more metal ions M^{2+}, often introduced in nonstoichiometric proportions, can provide great versatility of the magnetic properties. Mn–Zn and Ni–Zn ferrites are the two basic families of mixed soft ferrites, where by tuning the relative concentrations of the metal ions and making suitable additions and thermal treatments, material tailoring to specific applications can be achieved. Although, as previously stressed, normal $ZnFe_2O_4$ has zero magnetic moment, its addition to the inverse $MnFe_2O_4$ or $NiFe_2O_4$ ferrites leads to an increase of the global saturation magnetization at 0 K. This can be understood, in terms of Néel's theory, as due to the parallel alignment of the magnetic moments of the Fe^{3+} ions in the B-sites of $ZnFe_2O_4$, which is enforced by antiferromagnetic coupling with the Fe^{3+} ion moments in the A sites. The price one has to pay for mixing is a progressive decrease of the Curie temperature with increasing the $ZnFe_2O_4$ proportion. This is due to the weakening of the A–B coupling, as summarized for the $Mn_{1-x}Zn_xFe_2O_4$ and $Ni_{1-x}Zn_xFe_2O_4$ Zn ferrites in Fig. 18 (37,38). The simple spinel ferrites, having cubic symmetry, generally display a negative value of the anisotropy constant K_1 ($\langle 111 \rangle$ easy axis). This negative anisotropy derives, according to the single ion model, from the sum of the opposite contributions of the Fe^{3+} ion moments occupying the A and B sites, where the negative K_{1B} term eventually prevails over the positive term K_{1A}. In the case of $CoFe_2O_4$, however, K_1 is large and positive ($\langle 100 \rangle$ easy axis), because of the predominant role played by the large spin-orbit coupling of the Co^{2+} ions (see Table 7). By acting on both the

Table 7. Properties of Some Basic Spinel Ferrites

	$n_{B,th}$	$n_{B,exp}$	I_s(T)	T_c(°C)	$\delta(10^3 \text{ kg/m}^3)$	$\rho(\Omega \cdot \text{m})$	$K_1(10^3 \text{ J/m}^3)$	$\lambda_s(10^{-6})$
$FeFe_2O_4$	4	4.1	0.603	585	5.24	10^{-5}	−12	40
$NiFe_2O_4$	2	2.3	0.340	585	5.38	10^2	−7	−26
$CoFe_2O_4$	3	3.7	0.534	520	5.29	10^5	200	−110
$MgFe_2O_4$	1	1.0	0.151	440	4.52	10^5	−4	−6
$MnFe_2O_4$	5	4.6	0.503	330	5.00	10^2	−4	−5

$FeFe_2O_4$, $NiFe_2O_4$ and $CoFe_2O_4$ are inverse spinel ferrites (Fe^{3+} cations in the tetrahedral A sites), $MgFe_2O_4$ is mostly inverse (90% of A sites occupied by Fe^{3+}, 10% by Mg^{2+}), $MnFe_2O_4$ is mostly normal (80% of A sites occupied by Mn^{2+}, 20% by Fe^{3+}). $n_{B,th}$ and $n_{B,exp}$ are the calculated and experimental magnetic moments at 0 K per formula unit (Bohr magnetons). $I_s \equiv$ saturation polarization at room temperature; $T_c \equiv$ Curie temperature; $\delta \equiv$ density; $\rho \equiv$ electrical resistivity; $K_1 \equiv$ anisotropy constant; $\lambda_s \equiv$ saturation magnetostriction.
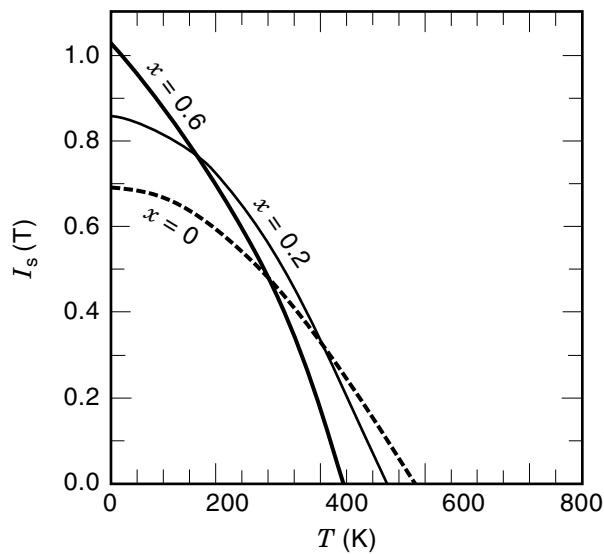
(a)
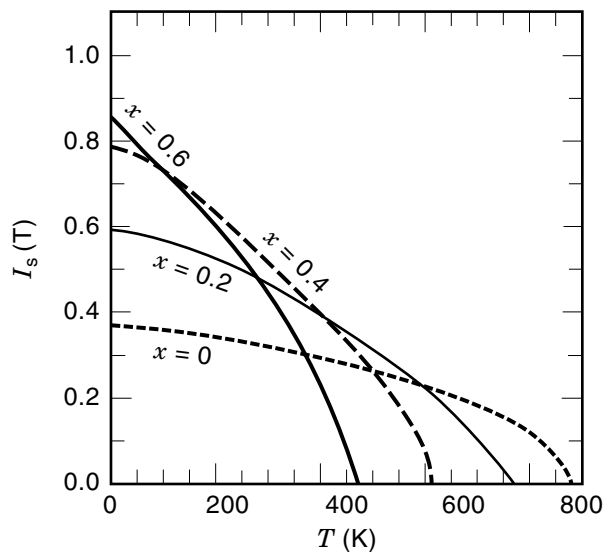
(b)

Figure 18. Effect of Zn substitution on the saturation magnetization and its temperature dependence in (a) $Mn_{1-x}Zn_xFe_2O_4$ ferrites (37) and (b) $Ni_{1-x}Zn_xFe_2O_4$ ferrites (38).

starting composition and the processing method, mixed Mn–Zn and Ni–Zn ferrites can actually be prepared having very low anisotropy values in a range of temperatures suitable for applications (20° to 100°C). It has been shown that Zn substitution in Mn and Ni ferrites leads, through weakening the exchange field acting on the B Fe ions, to a corresponding weakening of the negative K_{1B} constant on approaching room temperature (39). If, in addition, calibrated replacement of divalent cations with Fe^{2+} or Co^{2+} ions is made, one can combine the related positive anisotropy with the negative K_1 value of the host in such a way that the resultant anisotropy constant K_1 will cross the zero value around a convenient temperature (e.g., room temperature). Full anisotropy compensation is, for example, obtained at 300 K with the composition $Mn_{.53}Zn_{.40}Fe^{2+}_{.07}Fe^{3+}_2O_4$. As previously stressed, a small anisotropy provides a straightforward way to soft magnetic behavior, as summarized by the following approximate relationships for coercivity and initial susceptibility

$$H_c \propto K^{1/2} \quad \chi_i^{rot} \propto \frac{I_s^2}{K} \quad \chi_i^{dw} \propto \frac{I_s^2 \cdot \langle s \rangle}{K^{1/2}} \qquad (5)$$

where χ_i^{rot} and χ_i^{dw} are the contributions to the initial susceptibility deriving from coherent rotation of the magnetization and domain wall displacements, respectively, and $\langle s \rangle$ is the average grain size (40). Besides the crystalline structure, applied and residual stresses and magnetic ordering induced by field annealing may contribute to the magnetic anisotropy. The effect of these various terms is summarized by the constant K in Eq. (5). According to this equation, the temperature stability of permeability, which is important in many applications, is determined by the dependence of I_s and K on temperature. This can be controlled by acting on the addition of Fe^{2+} (mainly in the Mn–Zn ferrites) or Co^{2+} (mainly in the Ni–Zn ferrite). The highest permeabilities are reached in the Mn–Zn ferrites, whereas somewhat lower values are obtained in the Ni–Zn ferrites. Conversely, the latter display much higher resistivities (some $10^7 \Omega \cdot$m versus $10^{-2} \Omega \cdot$m to ~10 $\Omega \cdot$m, depending on the amount of doping with Fe^{2+} in Mn–Zn ferrites). The near-insulating character of ferrites is conducive to a nearly constant value of the initial susceptibility over many frequency decades, typically up to the megahertz region in Mn–Zn and the 100 MHz region in Ni–Zn ferrites, respectively. This is illustrated in Fig. 19, where the behavior versus frequency of the real and imaginary parts of the relative initial permeability $\mu = \mu' + i\mu''$ are presented for selected industrial products (41). In the low induction regimes and at sufficiently high frequencies the dissipation of energy can be
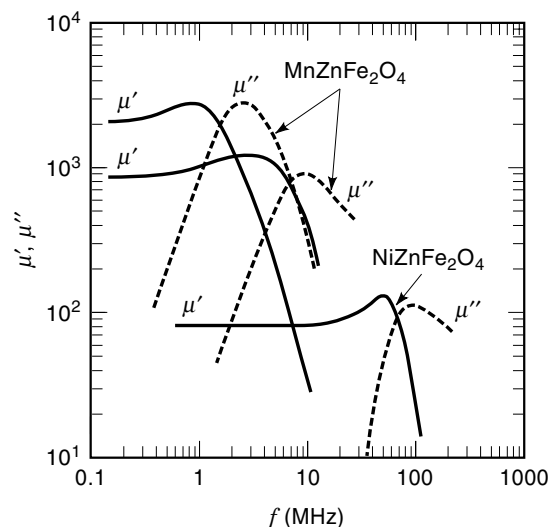
Figure 19. Frequency dependence of the real (μ') and imaginary (μ'') components of the initial permeability in selected industrial Mn–Zn and Ni–Zn ferrite samples (41).

related to the phase shift δ between $B(t)$ and $H(t)$ according to the equations

$$\tan \delta = \frac{\mu''}{\mu'} \quad W = \pi B_p H_p \frac{\tan \delta}{\sqrt{1 + \tan^2 \delta}} \tag{6}$$

where W is the energy loss per unit volume and the field and the induction have peak amplitude H_p and B_p, respectively. Besides possible damping effects by eddy currents, which in anisotropy-compensated Mn–Zn ferrites critically depend on the addition of Fe^{2+} ions, resonant absorption of energy is invoked for the high frequency losses. In any case, whatever the predominant magnetization mechanism, either coherent magnetization rotation or domain wall displacements, it appears that high susceptibility and high limiting frequency of operation are conflicting requirements (see Fig. 19). By denoting with f_0 the relaxation frequency, it is predicted, in particular, that for spin rotations $f_0\chi_i^{rot} \propto I_s$ and for domain wall processes $f_0\chi_i^{dw} \propto I_s^2/\langle s\rangle$ (42). This suggests that the dispersion of the susceptibility is shifted towards higher frequencies in small grained ferrites. The accurate control of the intrinsic and structural properties of spinel ferrites (e.g., ion valence, stoichiometry, grain size, porosity) during material preparation is accomplished through the well established routes of powder metallurgy.

The conventional production process starts with the preparation of the base oxides, typically by calcination of suitable iron salts, and their mixing by prolonged wet grinding. This leads to a homogeneously fine powder, where the dimension of the single granules is approximately 1 μm or less. The resulting mixture is then dried and prefired in air at 900° to 1200°C. During this stage the spinel ferrite is formed by solid state reaction of Fe_2O_3 with the other present metal oxides (MO or M_2O_3). The so-prepared powders are then compacted, either by die-punching or hydrostatic pressing, and pieces of the desired shape are obtained. The filling factor of the so-obtained assembly of particles is around 50% to 60%. In the final main step, the pieces are brought to a temperature of 1200° to 1400°C in an oxidizing atmosphere, with or without application of external pressure, so as to achieve the desired final magnetic and structural properties of the material through: (a) particle bonding by interdiffusion and grain growth; (b) densification, by elimination of the interparticle voids, up to ~95% to 98% filling factor; (c) chemical homogenization by completion of unfinished reactions. The resulting product is hard and brittle and, if required, it is eventually machined with precision abrasive tools in order to meet the final tolerances.

BIBLIOGRAPHY

1. W. F. Barrett, W. Brown, and R. A. Hadfield, Electrical conductivity and magnetic permeability of various alloys of Fe, *Sci. Trans. R. Dublin Soc.,* **7**: 67–126, 1900.

2. G. W. Elmen, *Magnetic material,* Canadian Patent No. 180, 359, 1916.

3. N. P. Goss, *Electrical sheet and method and apparatus for its manufacture and test,* U.S. Patent No. 1,965,559, 1933.

4. J. L. Snoek, Magnetic material and core, US patent 2,452,531, 1948.

5. L. Néel, Bases d'une nouvelle théorie générale du champ coercitif, *Ann. Univ. Grenoble,* **22**: 299–319, 1946.

6. R. Alben, J. J. Becker, and M. C. Chi, Random anisotropy in amorphous ferromagnets, *J. Appl. Phys.,* **49**: 1653–1658, 1978.

7. H. J. Williams, W. Shockley, and C. Kittel, Studies of the propagation velocity of a ferromagnetic domain boundary, *Phys. Rev.,* **80**: 1090–1094, 1950.

8. G. Bertotti, General properties of power losses in soft ferromagnetic materials, *IEEE Trans. Magn.,* **24**: 621–630, 1988.

9. K. Ueno, I. Tachino, and T. Kubota, Advantages of vacuum degassing of non-oriented electrical steels, in R. Pradham (ed.), *Metallurgy of Vacuum Degassed Steel Products,* Warrendale, PA: Mineral, Metals and Materials Soc., 1990, pp. 347–350.

10. G. Lyudkovsky and P. K. Rastogi, Effects of boron and zirconium on microstructure and magnetic properties of batch annealed Al-killed low carbon steels, *IEEE Trans. Magn.,* **21**: 1912–1914, 1985.

11. E. T. Stephenson, Effects of thickness and resistivity on core loss and permeability of nonoriented semiprocessed steels, *J. Appl. Phys.,* **55**: 2142–2144, 1984.

12. M. Shiozaki and Y. Kurosaki, The effects of grain size on the magnetic properties of nonoriented electrical steel sheets, *J. Mater. Eng.,* **11**: 37–43, 1989.

13. H. Shimanaka et al., Non-oriented Fe–Si steels useful for energy efficient electrical apparatus, in A. R. Marden and E. T. Stephenson (eds.), *Energy Efficient Electrical Steels,* Warrendale, PA: Metallurgical Soc. of AIME, 1980, pp. 193–204.

14. P. Brissonneau, J. Quenin, and J. Verdun, A new sheet with a pseudo-cubic texture for application to large rotating machines, *Proc. 7th Soft Magn. Mater. Conf.,* The Univ. College, Cardiff, 1985, pp. 209–211.

15. T. Yamamoto et al., Magnetic properties of grain-oriented silicon steels with high permeability Orientcore HI-B, *IEEE Trans. Magn.,* **8**: 677–681, 1972.

16. I. Goto et al., Development of a new grain-oriented silicon steels "RG-H" with high permeability, *Proc. 2nd Soft Magn. Mater. Conf.,* The Univ. College, Cardiff, 1975, pp. 262–268.

17. H. C. Fiedler, A new high induction grain-oriented 3% silicon–iron, *IEEE Trans. Magn.,* **13**: 1433–1436, 1977.

18. T. Nozawa, M. Yabumoto, and Y. Matsuo, Studies of domain refining of grain-oriented silicon steel, *Proc. 7th Soft Magn. Mater. Conf.,* The Univ. College, Cardiff, 1985, pp. 131–136.

19. K. I. Arai, K. Ishiyama, and H. Mogi, Iron loss of tertiary recrystallized silicon–steel, *IEEE Trans. Magn.,* **25**: 3949–3954, 1989.

20. D. Kohler, Promotion of cubic grain growth in 3% silicon iron by control of annealing atmosphere composition, *J. Appl. Phys.,* **31**: 408S–409S, 1960.

21. T. Yamaji et al., Magnetic properties and workability of 6.5% silicon steel sheet manufactured in continuous CVD siliconizing line, *J. Magn. Magn. Mater.,* **133**: 187–189, 1994.

22. J. C. Perrier and P. Brissonneau, Some physical and mechanical properties of SiAlFe alloys, *J. Magn. Magn. Mater.,* **26**: 79–82, 1982.

23. T. Masumoto et al., Production of Pd–Cu–Si amorphous wires by melt spinning method using rotating water, *Scripta Met.,* **15**: 293–296, 1981.

24. R. C. O'Handley, Fundamental magnetic properties, in F. E. Luborsky (ed.), *Amorphous Metallic Alloys,* London: Butterworths, 1983, pp. 257–282.

25. H. Kronmüller, N. Moser, and T. Reininger, Magnetization processes domain patterns and microstructure in amorphous alloys, *An. Fis.,* **B86**: 1–6, 1990.

26. M. Yagi et al., Very low loss ultrathin Co-based amorphous ribbon cores, *J. Appl. Phys.,* **64**: 6050–6052, 1988.

27. V. R. V. Ramanan, Metallic glasses in distribution transformer applications: An update, *J. Mater. Eng.,* **13**: 119–127, 1991.

28. C. H. Smith, Applications of rapidly solidifed soft magnetic alloys, in H. H. Liebermann (ed.), *Rapidly Solidified Alloys,* New York: Dekker, 1983, pp. 617–663.

29. G. Bertotti et al., Magnetic properties of rapidly quenched soft magnetic materials, *Mater. Sci. Eng.,* **A226–A228**: 603–613, 1997.

30. Y. Yoshizawa, S. Oguma, and K. Yamauchi, New Fe-based magnetic alloy composed of ultrafine grain structure, *J. Appl. Phys.,* **64**: 6044–6046, 1988.

31. A. Makino, A. Inoue, and T. Masumoto, Nanocrystalline soft magnetic Fe–M–B (M = Zr, Hf, Nb) alloys produced by crystallization of amorphous phase, *Mater. Trans. JIM,* **36**: 924–938, 1995.

32. G. Herzer, Grain size dependence of coercivity and permeability in nanocrystalline ferromagnets, *IEEE Trans. Magn.,* **26**: 1397–1402, 1990.

33. G. Couderchon and J. F. Tiers, Some aspects of magnetic properties of Ni–Fe and Co–Fe alloys, *J. Magn. Magn. Mater.,* **26**: 196–214, 1982.

34. J. Smit and H. P. J. Wijn, *Ferrites,* New York: Wiley, 1959.

35. L. Néel, Proprietés magnétiques des ferrites: Ferrimagnétisme et antiferromagnétisme, *Ann. Phys.,* **3**: 137–198, 1948.

36. P. W. Anderson, Antiferromagnetism, Theory of superexchange interaction, *Phys. Rev.,* **79**: 350–356, 1950.

37. C. Guillaud, Proprietés magnétiques des ferrites, *J. Phys. Radium,* **12**: 239–248, 1951.

38. R. Pauthenet, Aimantation spontanée des ferrites, *Ann. Phys.,* **7**: 710–745, 1952.

39. A. Broese Van Groenou, J. A. Schulkes, and D. A. Annis, Magnetic anisotropy of some nickel zinc ferrite crystals, *J. Appl. Phys.,* **38**: 1133–1134, 1967.

40. A. Globus, Magnetization mechanisms and specific polycrystalline properties in soft magnetic materials, *Proc. 2nd Soft Magn. Mater. Conf.,* Cardiff, 1975, pp. 233–248.

41. D. Stoppels, Developments in soft magnetic power ferrites, *J. Magn. Mater.,* **160**: 323–329, 1996.

42. R. Lebourgeois et al., Permeability mechanisms in high frequency polycrystalline ferrites, *J. Magn. Mater.,* **160**: 329–332, 1996.

F. FIORILLO
G. BERTOTTI
C. APPINO
M. PASQUALE
Istituto Elettrotecnico Nazionale
Galileo Ferraris

SOFTWARE.   See SPREADSHEET PROGRAMS.